

# Lithium in Wide Binaries: Effective Temperature Governs Depletion while Rotation Plays a Minor Role

CHENG-CHENG, XIE,<sup>1,2</sup> HAI-JUN, TIAN,<sup>1,2</sup> JIAN-RONG SHI,<sup>3,4</sup> AND ZE-MING ZHOU<sup>3,4</sup>

<sup>1</sup>*School of Sciences, Hangzhou Dianzi University, Hangzhou 310018, People's Republic of China*

<sup>2</sup>*Zhejiang Branch of National Astronomical Data Center, Hangzhou 310018, China*

<sup>3</sup>*National Astronomical Observatories, Chinese Academy of Sciences, Beijing 100101,*

<sup>4</sup>*University of Chinese Academy of Sciences, Beijing 100049, People's Republic of China*

## ABSTRACT

Using a sample of 116 wide binary systems as coeval and chemically homogeneous stellar pairs, we investigate the factors governing lithium depletion in main-sequence stars. We recover the well-established morphology of the lithium–effective temperature ( $T_{\text{eff}}$ ) relation, including the Li dip (6200–6600 K), the Li plateau (6000–6200 K), and a linear trend for cooler stars ( $T_{\text{eff}} < 6000$  K), where lithium abundance increases by  $\sim 0.15$  dex per 100 K. We demonstrate that the apparent correlation between projected rotational velocity ( $v \sin i$ ) and lithium abundance is secondary to the underlying  $T_{\text{eff}}$  dependence;  $v \sin i$  is not an independent driver of lithium depletion in our sample. Notably, we identify an anomalous system within the Li dip where the primary star exhibits a  $\sim 1.4$  dex lithium excess compared to its secondary companion at nearly identical  $T_{\text{eff}}$ . We discuss two plausible origins for this anomaly: external enrichment via planetesimal accretion or planetary engulfment, and binary interactions with an unresolved tertiary companion. Our results confirm  $T_{\text{eff}}$  as the dominant parameter controlling lithium depletion, while highlighting that additional, non-standard processes can occasionally produce significant lithium enrichment.

*Keywords:* Wide Binaries (251) — Lithium Abundance — History of astronomy(1868) — Interdisciplinary astronomy(804)

## 1. INTRODUCTION

Lithium (Li) is a key diagnostic element in stellar astrophysics. Its surface abundance, denoted as  $A(\text{Li})$ <sup>5</sup>, is readily destroyed by proton capture at temperatures exceeding  $2.5 \times 10^6$  K via  ${}^7\text{Li}(p,\alpha){}^4\text{He}$  (Burbidge et al. 1957; Bodenheimer 1965). Consequently, Li survives only in the outer layers of stars, making it a sensitive tracer of internal mixing and transport processes that connect the surface to hotter interiors. Standard stellar evolutionary theory (SSET; Deliyannis et al. 1990), which primarily considers convection and pre-main-sequence burning, for G-type dwarfs such as the Sun and cooler K-type dwarfs, models predict significant early lithium depletion, as their deep convective zones transport surface material into hot interior regions where lithium is rapidly destroyed via nuclear burn-

ing. This process is expected to occur predominantly during the pre-main sequence phase. In contrast, hotter F- and A-type stars possess substantially shallower convective envelopes; consequently, SSET predicts that their surface lithium abundances should remain relatively unchanged throughout their main-sequence lifetimes. However, SSET fails to reproduce key observational patterns of Li depletion in main-sequence stars. These include the pronounced “Li Dip” in mid-F dwarfs (Boesgaard & Tripicco 1986; Balachandran 1995), the relatively constant “Li Plateau” in late-F to early-G dwarfs, and the severe mass-dependent depletion observed in cooler G- and K-dwarfs (Cummings et al. 2017). Observations of Li in open clusters of different ages show that G dwarfs continue to deplete Li during the main sequence, in sharp contrast to the SSET (Soderblom et al. 1993; Pinsonneault 1997). The discrepancy between the SSET predictions and observations reveals the action of additional physical mechanisms not included in standard models.

Corresponding author: Hai-Jun Tian, Jian-Rong Shi  
hjtian@hdu.edu.cn, sjr@bao.ac.cn

<sup>5</sup>  $A(\text{Li}) = \log[N(\text{Li})/N(\text{H})] + 12$

To explain these discrepancies, rotational mixing induced by stellar spin-down has emerged as a leading candidate for the dominant non-standard Li depletion mechanism across spectral types (Pinsonneault et al. 1989; Ryan & Deliyannis 1995; Pinsonneault 1997; Sun et al. 2023). The loss of angular momentum drives internal circulation and shear instabilities, which transport surface Li to deeper, hotter regions, where it is destroyed. This framework is supported by correlations between Li abundance and rotation, where slower rotators typically show higher Li depletion (Pinsonneault 1997). Other processes such as atomic diffusion (Richer 1993), mixing induced by internal gravity waves (García López & Spruit 1991), and matter accretion (Li et al. 2025) may also contribute to the observed scatter in Li abundances at a given effective temperature ( $T_{\text{eff}}$ ) and metallicity. Additional evidence comes from the correlation of spindown to Li depletion (Steinhauer & Deliyannis 2025), and from stars such as short period tidally locked binaries with higher Li than normal, single stars (Ryan & Deliyannis 1995). Inside stars, Li, Be, and B survive to progressively deeper layers. By far the most powerful observational constraints on physical processes affecting Li depletion come from incorporating information from Be and B abundances as well, especially from the observed ratios of these elements (Boesgaard et al. 2020; Deliyannis et al. 1998; Boesgaard et al. 2005).

The efficiency of all these depletion mechanisms is fundamentally modulated by the structure of the stellar interior, particularly the depth of the surface convection zone (SCZs, Pinsonneault 1997). The depth of SCZ increases with decreasing stellar mass (and  $T_{\text{eff}}$ ), leading to more efficient transport of Li to its destruction region. This explains the general trend of increasing Li depletion from F- to K-dwarfs. The Li Dip (approximately 6200–6800 K) corresponds to a narrow mass range where the SCZ reaches a critical depth, often coupled with the onset of efficient rotational braking (Théado & Vauclair 2003), resulting in severe Li depletion. The Li Plateau (approximately 6000–6200 K) represents a transition regime where the SCZ is relatively shallow, allowing Li to be preserved at near-primordial levels in some populations. In cooler stars ( $T_{\text{eff}} < 6000$  K), the deep SCZ leads to efficient Li destruction throughout the main sequence.

Metallicity further influences Li depletion through multiple channels. Higher metallicity increases atmospheric opacity, leading to a deeper SCZ at a given  $T_{\text{eff}}$ , which enhances convective mixing and the destruction of Li. Additionally, metallicity affects stellar structure, rotational evolution, and the efficiency of atomic diffusion processes (Pinsonneault 1997; Ryan 2000). These

metallicity-dependent effects contribute to the observed variations in Li patterns between metal-rich and metal-poor stellar populations.

Wide binaries (WBs), defined as gravitationally bound stellar pairs with large separations ( $\gtrsim 100$  AU), provide a powerful laboratory for isolating the effects of these physical mechanisms. Components of a WB are coeval and share a common initial chemical composition, having formed from the same molecular cloud core. High-resolution spectroscopic studies have robustly confirmed their chemical homogeneity, particularly for refractory elements (Hawkins et al. 2020). However, despite these identical initial conditions, WB components often exhibit significant differences in their surface Li abundances. These differences must therefore arise from internal stellar properties that have diverged during their evolution, such as mass (and hence  $T_{\text{eff}}$ ), rotation, and convective efficiency—precisely the parameters that govern Li depletion. This makes WBs an ideal testbed for disentangling the various proposed depletion mechanisms, free from the confounding variables of age and initial composition that affect comparisons between field stars or even star clusters.

Recent studies of large samples of co-moving stellar pairs have quantified the intrinsic scatter in  $A(\text{Li})$  at fixed  $T_{\text{eff}}$  and metallicity, finding values of  $\sim 0.35$  dex for solar-type stars (Sun et al. 2025b). This scatter likely reflects the complex interplay of rotation, magnetic activity, and other internal processes. In particular, such studies also suggest that potential Li enrichment signatures from rare events such as planetary engulfment are often of similar amplitude to this intrinsic scatter, making them challenging to distinguish observationally (Sevilla et al. 2022; Sun et al. 2025b). Therefore, analyzing systems with extreme Li anomalies, such as a component within a coeval pair showing an unusually high abundance, becomes crucial for identifying clear signatures of non-standard processes.

In this work, we perform a detailed analysis of lithium abundances in a sample of WBs. Our primary goals are to: (1) map the  $A(\text{Li})$ - $T_{\text{eff}}$  relation in a coeval chemically homogeneous environment; (2) investigate the roles of  $T_{\text{eff}}$  (mass) and rotation in driving depletion; and (3) identify and scrutinize any systems exhibiting anomalous Li abundances that may point to specific events such as external enrichment. Our sample is constructed from *Gaia* EDR3 wide binary catalogs, with atmospheric parameters and high-resolution spectra drawn from GALAH DR3 (Buder et al. 2021).

This paper is structured as follows. Section 2 describes the selection of our WB sample and the spectroscopic data. Section 3 details the methodology for determining

Li abundances via spectral synthesis. Our main results, including the  $A(\text{Li})-T_{\text{eff}}$  pattern and the analysis of an anomalous system, are presented in Section 4. In Section 5, we discuss the implications of our findings and propose mechanisms to explain the observed Li anomaly. Finally, our conclusions are summarized in Section 6.

## 2. DATA AND ANALYSIS

### 2.1. *The Initial Wide Binaries Sample from Gaia*

This study uses the initial catalog of wide binary candidates identified by El-Badry et al. (2021) from *Gaia* Early Data Release 3 (*Gaia* EDR3, Gaia Collaboration et al. 2021). The selection of candidates was constrained to sources nominally within a distance limit of 1 kpc. The identification methodology closely followed the approaches established by El-Badry & Rix (2018) and Tian et al. (2020). This involved applying stringent criteria based on the parallax, proper motion, astrometric solution quality, and photometric properties of both stellar components within each candidate pair. Subsequent processing steps aimed to mitigate contamination by excluding cluster members, background projection pairs, and higher-order multiples (e.g., triples). For details on specific selection thresholds and filtering procedures, refer to Section 2 of El-Badry et al. (2021). We use the 877,416 high bound probability Main Sequence - Main Sequence (MSMS) wide binaries as our initial sample.

### 2.2. *Wide Binaries Cross-matched with GALAH*

The Galactic Archeology with HERMES (GALAH) survey’s Data Release 3 (DR3; Buder et al. 2021) provides one-dimensional spectra, stellar atmospheric parameters, and individual elemental abundances for 678,423 high resolution spectra ( $R \approx 28000$ ) of 588,571 individual objects. They were observed with the HERMES spectrograph at the Anglo-Australian Telescope. The survey provides uniformly derived stellar parameters, such as effective temperature ( $T_{\text{eff}}$ ), surface gravity ( $\log g$ ), metallicity ( $[\text{Fe}/\text{H}]$ ), micro-turbulent velocity ( $\xi_t$ ),  $v \sin i$ , and  $R_V$ , they were derived by using a modified version of the spectrum synthesis code Spectroscopy Made Easy (SME) and 1D MARCS model atmospheres. We got 218 pair spectra by cross-matching the initial MSMS binary sample with the GALAH DR3 catalogue. In addition, the GALAH DR3 provided the strict data quality flags (the values of those flags equal to 0 means that the parameters are reliable) of the stellar parameters and elemental abundances, to ensure the accuracy of the results. In this paper only the spectra quality parameters of "flag\_sp=0" and "fe\_h\_sp=0" have been considered.

We have limited the difference in  $\Delta R_V$  (and  $\Delta[\text{Fe}/\text{H}]$ ) (i.e., the difference  $R_V$  or  $[\text{Fe}/\text{H}]$  between the two components of each binary), and removed the sources of  $\Delta R_V$  (and  $\Delta[\text{Fe}/\text{H}]$ ) beyond  $\pm 3 \sigma_{R_V}$  (and  $\pm 3 \sigma_{[\text{Fe}/\text{H}]}$ ). Finally, we obtained a sample of 116 binary systems, and their observational properties and atmospheric parameters are listed in Table A1.

Although GALAH DR3 and DR4 provided valuable homogeneously derived catalogs of stellar parameters and elemental abundances—including Li (Buder et al. 2021; Buder et al. 2024), we would like to perform an independent measurement of Li abundance for this study. This choice is prompted by noted inconsistencies between the two data releases, particularly a reported decrease in precision for certain abundances in DR4 (Buder et al. 2025). The differences stem from a substantial change in methodology: GALAH DR3 employed classical spectral synthesis with Spectroscopy Made Easy (Piskunov & Valenti 2017; Buder et al. 2021), while DR4 adopted a neural-network approach trained on synthetic spectra (Kane et al. 2025). In both data releases, there exist some stars for which effective Li abundances are not provided. Due to these reasons, the Li abundances presented in the remainder of this work are based on our own dedicated spectral re-analysis.

## 3. MEASUREMENT OF LITHIUM ABUNDANCE

### 3.1. *Li abundance*

We adopt the stellar atmospheric parameters of stars, i.e., the effective temperature  $T_{\text{eff}}$ , surface gravity  $\log g$ , metallicity  $[\text{Fe}/\text{H}]$ , and microscopic turbulence velocity  $\xi_t$ , from GALAH DR3 (Buder et al. 2021). The Li abundances are derived under both the local thermodynamic equilibrium (LTE) and non-local thermodynamic equilibrium (NLTE) assumptions using the spectral synthesis method. The LTE and NLTE Li abundances are determined from the resonance line at 6708 Å via the spectral synthesis method, which interactively finds the best matches between observed and synthetic spectra. Synthetic line profiles are calculated using the IDL/Fortran-based Spectrum Investigation Utility (SIU, Reetz 1999) program with the 1D LTE MARCS atmospheric models (Gustafsson et al. 2008). In our analysis, the adopted Li line data and the atomic model have been presented in detail by Shi et al. (2007). To solve the coupled radiative transfer and statistical equilibrium equations, a revised DETAIL code (Mashonkina et al. 2011) is employed, which uses an accelerated  $\Lambda$ -iteration method (Rybicki & Hummer 1991, 1992). During the fitting procedures, free parameters are the Li abundance and a Gaussian profile, which accounts for instrumental, rotational, and macro-turbulent broadening. Figure 1 (left

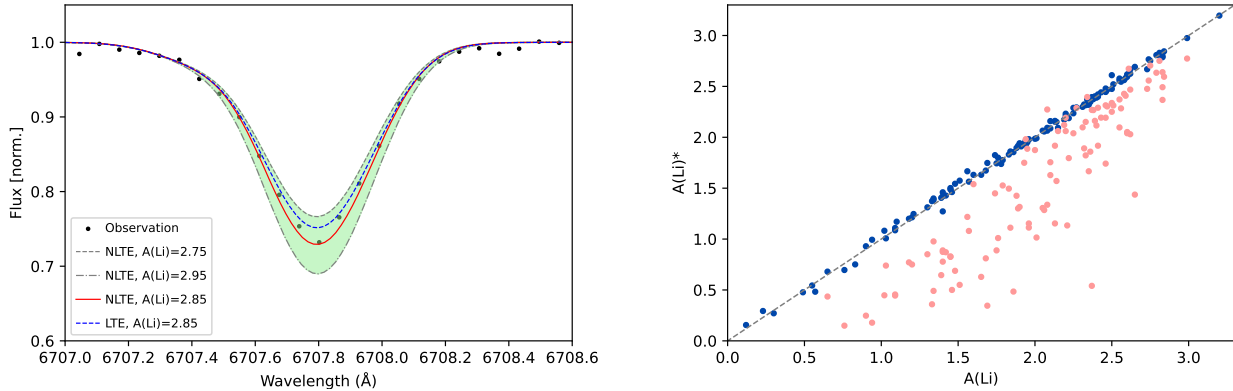


**Figure 1.** Left panel: An example for  $A(\text{Li})$  measurement. The black points are the observed spectra, and the red line is the best fit synthetic spectra with  $A(\text{Li})=2.85$  dex. The gray dashed and dotted lines are the uncertainties of the fitting with  $A(\text{Li})=2.75$  dex and 2.95 dex, respectively. Right panel: The abscissa represents the Li abundance determined by us, while the ordinate represents the Li abundance provided by GALAH DR3 (blue points) or GALAH DR4 (red points).

panel) shows an example of the spectral synthesis fitting. The measured  $A(\text{Li})$  of the 116 binary systems is given in Table A1, including 61 (65) systems of which  $A(\text{Li})$  is not provided by GALAH DR3 (DR4).

### 3.2. The Uncertainties of Our Li Abundances

The abundance of Li is sensitive to stellar atmospheric parameters, in particular of temperature. Thus, it is important to investigate the uncertainty in Li abundance as a result of the uncertainties in the stellar parameters. The uncertainty of Li abundance is quantified by the changes in their errors for the four stellar parameters, i.e.,  $T_{\text{eff}}$ ,  $\log g$ ,  $[\text{Fe}/\text{H}]$ , and  $\xi_t$ . As an example, the uncertainties of the abundance of Li due to the errors in the stellar parameters for WB05a are shown in Table 1. The results indicate that, among the considered sources of uncertainty, errors in  $T_{\text{eff}}$  have the most significant impact on  $A(\text{Li})$ , while the contributions from other parameters are negligible within their respective uncertainty ranges. For our sample, where the typical  $T_{\text{eff}}$  uncertainty is 70–80 K, this propagates to a measurement uncertainty in  $A(\text{Li})$  of approximately 0.05–0.06 dex.

### 3.3. The Validation of Our Li Abundances

To validate the measured  $A(\text{Li})$ , we compare the derived  $A(\text{Li})$  with those from GALAH DR3 and DR4. The right panel of Figure 1 shows that our  $A(\text{Li})$  is well in agreement with the values of GALAH DR3, while systematically higher than those of GALAH DR4. This comparison confirms that our measured  $A(\text{Li})$  is reliable.

## 4. RESULTS

The coeval and co-natal nature of WBs ensure that the component stars share consistent metallicity and age.

**Table 1.** The uncertainties of measured  $A(\text{Li})$  due to the errors in the stellar parameters of WB05a

Atmo.	$T_{\text{eff}}$ (K)	$\log g$ (dex)	$[\text{Fe}/\text{H}]$ (dex)	$\xi_t$ ( $\text{km s}^{-1}$ )
Mean	5892	4.2	0.3	1.2
Error	+72 -72	+0.2 -0.2	+0.05 -0.05	+0.1 -0.1
$\Delta A(\text{Li})$	+0.06 -0.05	+0.01 0.00	+0.01 0.00	0.00 0.00

NOTE—The uncertainties in  $A(\text{Li})$  are derived from propagating the errors in stellar parameters through spectral synthesis analysis.

As the fundamental parameters are well-constrained, WBs offer an ideal laboratory for investigating which factors will influence the stellar Li abundance  $A(\text{Li})$ .

Figure 2 plots Li abundances as a function of the effective temperature for our binary sample. The upper panel presents  $A(\text{Li})$  against  $T_{\text{eff}}$  for all 116 systems, with each binary pair connected by a black dashed line. Individual components are represented by filled circles, color-coded by  $[\text{Fe}/\text{H}]$  and scaled in size according to their  $v \sin i$  values. The bottom panel displays the differential quantities  $\Delta A(\text{Li})$  versus  $\Delta T_{\text{eff}}$ , defined as the difference between the primary and secondary components of each pair. Here, symbols are color-coded by the  $T_{\text{eff}}$  of the secondary star and their size scales with  $|\Delta v \sin i|$ .

It is difficult to find the influences of  $[\text{Fe}/\text{H}]$  on  $A(\text{Li})$  due to the co-natal nature between two components of an individual WB and the narrow range ( $-0.4 < [\text{Fe}/\text{H}] < 0.2$  dex) of metallicity in our sample. Therefore, in this section, we systematically explore the

effects of effective temperature ( $T_{\text{eff}}$ ) and stellar rotation ( $v \sin i$ ) on the observed Li abundances.

#### 4.1. $T_{\text{eff}}$ : A Key Controlling Factor for Lithium Depletion

As Figure 2 shows, our data reveal a strong correlation between  $A(\text{Li})$  and  $T_{\text{eff}}$ , characterized by three distinct regimes: the Li dip (6200–6600 K), the Li plateau (6000–6200 K), and a clear linear trend in the cooler binaries ( $T_{\text{eff}} < 6000$  K)—where the connecting lines generally share a consistent slope.

##### 4.1.1. Li Dip (6200 K – 6600 K)

The upper panel of Figure 2 shows a pronounced Li dip feature in the  $T_{\text{eff}}$  range 6200–6600 K. Within binary systems, Li depletion becomes increasingly severe toward the center of this range, reaching a minimum near 6500 K. This morphology—lower  $A(\text{Li})$  in the center and higher values toward both hotter and cooler edges—is consistent with the classical Li dip observed in intermediate age and old open clusters.

In particular, a binary system in our sample exhibits an intriguing deviation: both components (connected by a red dashed line) have  $T_{\text{eff}} \sim 6500$  K, a temperature near the bottom of the Li dip valley where the lowest  $A(\text{Li})$  values are expected. In contrast to this expectation, the primary star shows unexpectedly high Li abundance. The values of its astrometry, atmospheric parameters, and Li abundance are given as WB01 in the first row of Table A1. We will discuss this exceptional case further in Section 5.

In the bottom panel of Figure 2, binaries whose components fall within the Li dip are marked by inverted triangles, color-coded by  $T_{\text{eff}}$  of the secondary star. The differential abundance of Li,  $\Delta A(\text{Li})$ , becomes more pronounced near the center of the dip (around  $\sim 6450$  K). In our sample, the absolute value of  $\Delta A(\text{Li})$  within the dip reaches a maximum of 1.65 dex, which rapidly decreases to 0.97 dex toward the edges of the temperature range.

##### 4.1.2. Li Plateau (6000 K – 6200 K)

The Li plateau appears as another distinct feature in the  $T_{\text{eff}}$  range of 6000–6200 K, as shown in the inset of the upper panel of Figure 2. To highlight this regime, the inset displays only binary pairs in which both components have  $T_{\text{eff}}$  between 5700 K and 6200 K. Across the plateau,  $A(\text{Li})$  remains roughly constant at an average value of about 2.5 dex, marked by the red dashed horizontal line spanning 5700–6200 K. This observed average is slightly lower than the theoretically predicted primordial Li abundance of  $A(\text{Li}) \sim 2.7$  dex from standard Big Bang nucleosynthesis. In the bottom panel

of Figure 2, these binary pairs are indicated by filled squares.

Notably, as shown in the inset in Figure 2, three binary systems in our sample exhibit slight deviations from the plateau. (1) In binary system WB02, the secondary star is a typical Li-plateau source with  $A(\text{Li}) \simeq 2.46$  dex, while the primary star shows a significantly lower abundance ( $A(\text{Li}) \simeq 1.49$  dex). This deviation likely occurs because the primary’s  $T_{\text{eff}}$  (6188 K) is near the Li-dip zone, causing it to exhibit Li-dip characteristics. (2) In binary system WB03, the secondary star ( $T_{\text{eff}} \simeq 6017$  K) lies close to the lower boundary (6000 K) of the Li plateau. Its Li abundance ( $A(\text{Li}) \simeq 1.03$  dex) is approximately 1.44 dex lower than that of the primary star. (3) In the WB04 binary system, both components deviate from the Li plateau, and the reason for this deviation remains unclear.

According to Sun et al. (2025b),  $A(\text{Li})$  shows a rapid decrease within  $\pm 100$  K around the solar  $T_{\text{eff}}$  ( $\sim 5777$  K). In our sample (upper panel of Figure 2), over this solar-like range (5677–5877 K), aside from a pronounced sharp drop for the two binary pairs highlighted by the orange line in the inset, no statistically significant steep decline is observed overall.

##### 4.1.3. Cool Stars (<6000 K)

A clear linear trend is observed for cooler binaries with  $T_{\text{eff}} < 6000$  K, as shown in the upper panel of Figure 2. The connecting lines exhibit a consistent slope across a wide  $\Delta T_{\text{eff}}$  range, exceeding 1200 K in some cases (bottom panel). The dashed black line represents a fit to the filled points (cool stars only), excluding symbols for Li dip binaries (inverted triangles), Li plateau binaries (filled squares), and systems where only the secondary is a cool star (crosses). The fitted slope of  $\sim 0.0015$  implies that for cool stars, a  $T_{\text{eff}}$  increase of 100 K corresponds to an increase of  $A(\text{Li})$  of approximately 0.15 dex, regardless of the binaries’ ages and metallicities. Although open clusters of different ages show significant scatter in the  $T_{\text{eff}}$  plane due to continued main-sequence depletion (Steinhauer & Deliyannis 2025), the relatively tight correlation in Figure 2 can be understood by considering the age distribution of our sample. Our wide binaries are field stars, with ages typically exceeding those of most open clusters. In such old G and K dwarfs, lithium depletion has effectively saturated, reducing the dispersion at a given  $T_{\text{eff}}$ . Thus, the tight trend reflects the convergence of lithium abundances in old stars, consistent with the idea that  $T_{\text{eff}}$  (via convection zone depth) is the primary parameter governing the final lithium abundance after several Gyr of evolution.

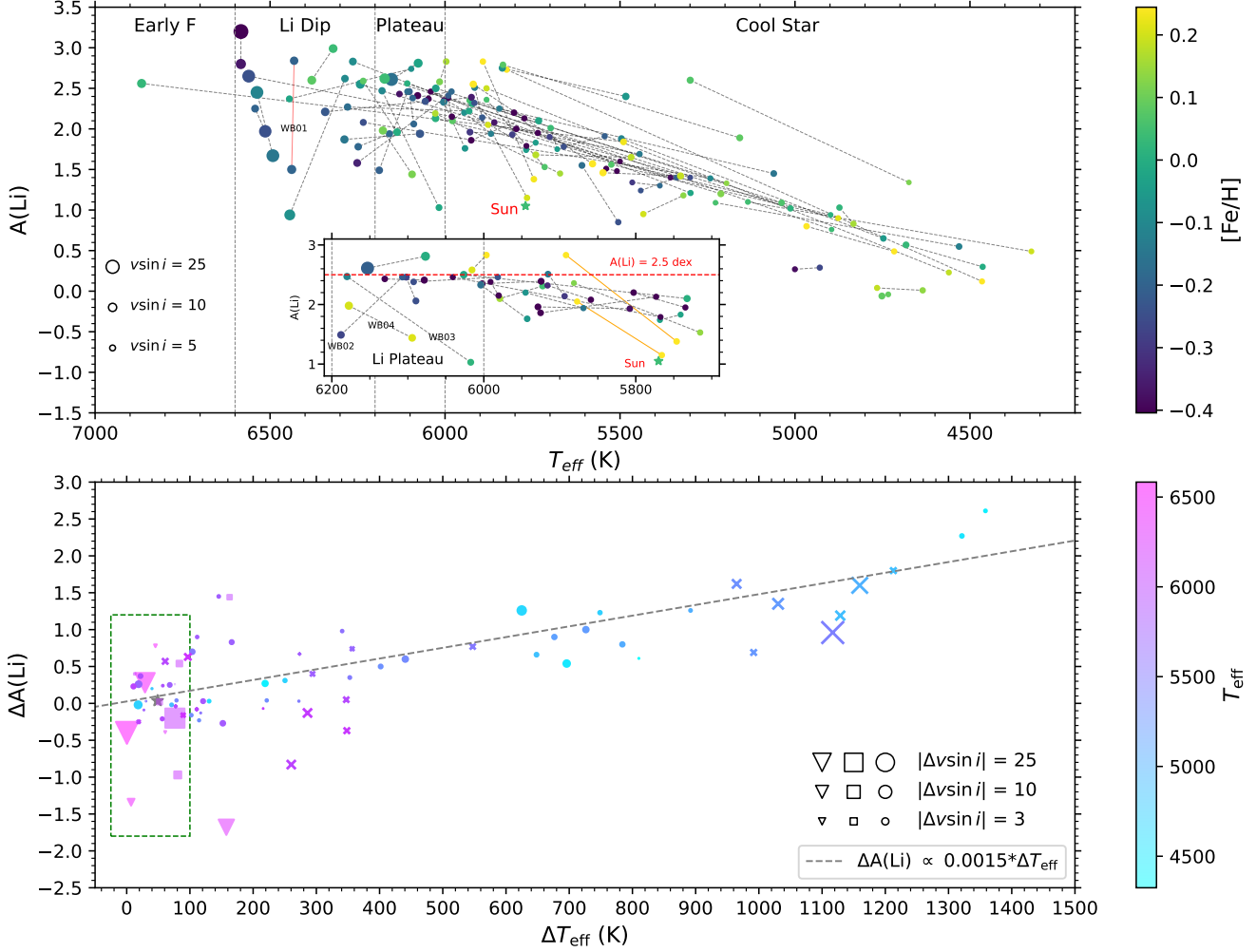


**Figure 2.** Upper: The 1D NLTE  $A(\text{Li}) - T_{\text{eff}}$  pattern for 116 pair WBs. Each binary pair is connected by a black dashed lines. Component stars are marked by filled circles which scaled in size according to their  $v \sin i$  values, and color-coded by their  $[\text{Fe}/\text{H}]$ , spanning the range of  $\langle [\text{Fe}/\text{H}] \rangle \pm 1.5\sigma$  (approximately  $-0.18 \pm 0.32$  dex). The inset zooms in on binary pairs where both components have  $T_{\text{eff}}$  between 5700 K and 6200 K. Bottom:  $\Delta A(\text{Li})$  as a function of  $\Delta T_{\text{eff}}$  between the primary and the secondary of each pair binary. The symbols are colored by the  $T_{\text{eff}}$  of the secondary stars. The symbols size are coded by the  $|\Delta v \sin i|$  between the primary and secondary stars. The dashed black line represents a linear fit to the filled points (cool stars only), excluding symbols for Li dip binaries (inverted triangles), Li plateau binaries (filled squares), and systems where only the secondary is a cool star (crosses). The green dashed box includes the binary pairs with negligible  $T_{\text{eff}}$  differences ( $\Delta T_{\text{eff}} < 100$  K). The black asterisk marks the median value of  $A(\text{Li})$  in the box.

According to Standard Stellar Evolution Theory, a star’s effective temperature dictates the depth of its SCZ. Cooler stars possess deeper SCZs because of their higher atmospheric opacity. A deeper SCZ enhances internal mixing, efficiently transporting Li from the surface to the hot interior, where it is destroyed. This process intensifies post-main-sequence. As the core contracts and the envelope expands, the star cools. The lower temperature increases the opacity (e.g., via neutral H and molecules such as TiO), forcing the outer layers to become more convective. The correlation between deeper SCZs in cooler stars and enhanced Li depletion

provides a theoretical basis for the observed depletion trend in our cool star sample.

#### 4.2. $v \sin i$ : Is A Dominant Driver for Lithium Depletion?

Figure 2 (upper panel) shows that stars hotter than 6000 K generally have higher projected rotational velocities ( $v \sin i$ ) and higher average Li abundances ( $A(\text{Li})$ ) than cooler stars. Specifically, hotter stars ( $T_{\text{eff}} > 6200$  K) show  $\langle v \sin i \rangle \sim 25 \text{ km s}^{-1}$ , while cooler stars ( $T_{\text{eff}} < 6000$  K) have  $\langle v \sin i \rangle \sim 5 \text{ km s}^{-1}$ . Although this may suggest a link between rotation and Li deple-

tion, our results indicate that the predominant effects are effective temperature.

We find no evidence in our sample that  $v \sin i$  independently controls Li depletion. This conclusion is supported by three key observational results:

1. **The correlation is secondary compared to  $T_{\text{eff}}$ :** Both  $v \sin i$  and  $A(\text{Li})$  scale with stellar mass, and hence  $T_{\text{eff}}$ . Hotter stars naturally rotate faster and retain more Li as a result of shallower convective zones. The apparent connection between higher  $v \sin i$  and higher  $A(\text{Li})$  is therefore a by-product of their common dependence on temperature.
2. **No clear relationship within individual binary pairs:** Even in the Li dip region, we find no systematic trend between  $v \sin i$  and  $A(\text{Li})$  within coeval pairs. Several systems show that the component with *higher*  $v \sin i$  has *lower*  $A(\text{Li})$ , contrary to the expectation that faster rotators should retain more Li.
3. **No correlation when  $T_{\text{eff}}$  is fixed:** For binary pairs with negligible  $T_{\text{eff}}$  differences ( $\Delta T_{\text{eff}} < 100 \text{ K}$ , enclosed by the green dashed box on the bottom panel), the mean  $\Delta A(\text{Li})$  is  $\sim 0.03 \pm 0.08 \text{ dex}$ . This holds even for the three pairs with large  $\Delta A(\text{Li})$  (marked with inverted triangles and squares), indicating that rotation does not lead to the observed lithium scatter.

These findings do not confirm the claim of Sun et al. (2025a) that faster rotators systematically retain higher  $A(\text{Li})$  with less scatter. Instead, within our sample, the available evidence does not support  $v \sin i$  as an independent dominant driver of the observed lithium depletion, and the dominant control appears to be  $T_{\text{eff}}$ .

## 5. DISCUSSION

As mentioned in Section 4.1.1, we identify an interesting binary system (WB01, connected by a red dashed line in Figure 2). Its primary star exhibits an unexpectedly high Li abundance ( $\sim 2.84 \text{ dex}$ ) near the bottom of the Li dip valley, approximately  $\sim 1.34 \text{ dex}$  greater than that of its secondary companion with nearly identical  $T_{\text{eff}}$ . This significant discrepancy warrants further exploration of possible underlying mechanisms. We discuss two plausible scenarios that may account for the observed Li enhancement in the primary star.

One possible explanation is external enrichment via planetesimal accretion or engulfment of hydrogen-poor planets. The elevated Li abundance of the primary

star could result from the accretion of external material rich in Li. Two related processes are considered: *planetesimal accretion* and *engulfment of hydrogen-poor planets*. In both cases, Li preserved in solid or planetary bodies is delivered to the stellar surface, altering its observed composition. Consequently, even a modest amount of accreted hydrogen-poor material can significantly enhance the surface abundances of Li and other elements. Planetesimal accretion involves the continuous or episodic accumulation of small solid bodies (e.g., asteroids or comet cores), while planetary engulfment is a more catastrophic event where an entire planet is assimilated. The observed Li excess in the primary star could thus reflect past accretion or engulfment events, possibly during the system’s early evolutionary stages. Further spectroscopic analysis of the ratios of refractory versus volatile elements could help distinguish between these scenarios (e.g., Nagar et al. 2019).

Another plausible explanation involves the presence of an unresolved companion and binary interaction effects. Photometric and isochronal analysis supports this: as shown in Figure 3, the secondary star aligns with a 1 Gyr isochrone (black solid line), while the primary star’s position is consistent with an unresolved binary system having a mass ratio of  $q = 0.7$  (the dashed black isochrone calculated according to Li et al. (2020)). This implies that the primary may have an unresolved companion of about  $0.7 M_{\text{primary}}$ . The unresolved companion could influence the primary’s Li abundance through several binary interaction pathways. For instance, tidal interactions in close binary systems can induce rotational mixing, enhancing Li depletion or production, depending on the specific angular momentum transport. Alternatively, mass transfer from the companion to the primary—either via Roche-lobe overflow or wind accretion—could deposit Li-rich material onto the primary’s surface. Such processes are known to alter the surface compositions in binary systems (e.g., in short-period tidally locked binaries; Deliyannis et al. 1994). However, the specific physical process through which an unresolved companion might enhance the primary’s Li abundance remains unclear and requires detailed modeling of binary evolution and internal mixing to elucidate. Additionally, the observed Li line strength itself could be affected by spectral contamination from the light of an unresolved companion, further complicating the interpretation. It is also important to note that this particular scenario—invoking an unresolved companion to explain Li enhancement—cannot account for other binary systems in our sample (e.g., WB02, WB03, and WB04). In those systems, the primary stars exhibit low Li abundances despite potentially hosting un-

resolved companions, indicating that the mere presence of a close companion does not systematically lead to Li enrichment.

In summary, the anomalous Li abundance in the primary star of this binary system can be attributed either to external enrichment (through planetesimal accretion or planetary engulfment) or to binary interactions involving an unresolved companion. Both hypotheses are plausible and align with broader findings in stellar astrophysics, particularly for A-type stars, where surface abundances are sensitive to external material and binary dynamics. Future high-resolution spectroscopic observations, coupled with detailed chemical abundance analysis and binary evolution modeling, will be essential to discriminate between these scenarios and uncover the origin of Li enhancement in such systems.

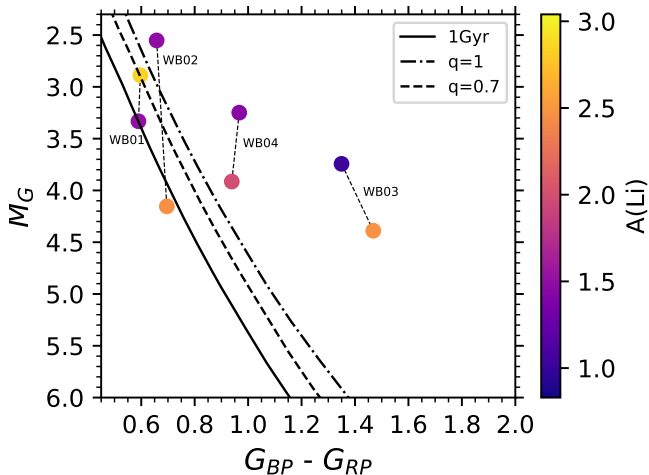


**Figure 3.** The Color-Magnitude Diagram (CMD) pattern of the anomalous systems (e.g., WB01, WB02, WB03 and WB04) that color-coded by their  $A(\text{Li})$  and connected by the dashed gray lines for the primary and secondary stars. The black solid line represents the 1 Gyr MS isochrone, and the dashed and dashed-dot black lines are the isochrones for unresolved binaries with  $q = 0.7$  and  $1.0$ , respectively. The  $q$  represent the mass ratio of an unresolved binary.

## 6. CONCLUSION

This study utilizes a sample of 116 wide binary systems as coeval and chemically homogeneous stellar pairs to investigate the factors governing Li depletion in main-sequence stars. The primary conclusions drawn from our analysis are as follows:

1. **Effective temperature ( $T_{\text{eff}}$ ) is the dominant factor controlling Li depletion:** (a) The well-established morphology of the Li- $T_{\text{eff}}$  relation is clearly recovered in our binary sample. The infiltration is most severe near its center around 6500 K; (b) the Li Plateau (6000–6200 K), where the abundances remain roughly

constant at an average  $A(\text{Li}) \sim 2.5$  dex; and (c) cooler stars ( $T_{\text{eff}} < 6000$  K), where  $A(\text{Li})$  exhibits a clear linear correlation with  $T_{\text{eff}}$ , increasing by  $\sim 0.15$  dex per 100 K increase. The consistent slopes of the connecting lines between binary components in a wide  $T_{\text{eff}}$  range reinforce that the depletion trend is primarily governed by temperature, likely through its control on the depth of SCZ and the efficiency of internal mixing.

2. **Projected rotational velocity ( $v \sin i$ ) is not an independent dominant driver of Li depletion in our sample:** Although hotter ( $> 6000$  K), faster-rotating stars show higher average Li abundances, this correlation is secondary to the underlying dependence on  $T_{\text{eff}}$ . No systematic relationship between  $v \sin i$  and  $A(\text{Li})$  is found within individual binary pairs of similar temperature, nor is a correlation present when the differences in  $T_{\text{eff}}$  are minimal ( $\Delta T_{\text{eff}} < 100$  K). Therefore, the observed link between rotation and Li abundances can best be explained by their common scaling with stellar mass and effective temperature, rather than a direct causal influence.

3. **An exceptional binary system within the Li dip presents a case for anomalous Li enrichment:** One system, with both components with  $T_{\text{eff}}$  near 6500 K, shows a  $\sim 1.4$  dex Li excess in its primary star compared to its secondary. Two plausible non-mutually exclusive origins are suggested for this anomaly: (i) external enrichment via accretion of planetesimals or engulfment of a hydrogen-poor planet, or (ii) binary interactions with an unresolved tertiary companion that could induce rotational mixing or mass transfer. Both scenarios are observationally motivated but require further verification through detailed chemical abundance analysis and binary evolution modeling.

In summary, our analysis of wide binaries confirms that stellar effective temperature is the principal parameter governing the observed pattern of Li depletion across a broad spectral range. The role of rotation appears to be subsidiary in this context. The identified anomalous system highlights that additional processes—such as external pollution or complex binary interactions—can occasionally override the standard depletion trends and merit targeted follow-up. Future studies combining high-resolution spectroscopy for detailed elemental abundances and precise orbital monitoring will be crucial to elucidate these exceptional cases and further refine our understanding of lithium evolution in stellar systems.

## ACKNOWLEDGMENTS

The authors thank Min Fang, Xiao-Ting Fu, Feng Wang, Lu Li and Xun-Zhou Chen for the helpful discussions. This work is supported by the Strategic Priority Research Program of Chinese Academy of Sciences, grant No. XDB1160101. This research is also supported by the National Natural Science Foundation of China under Grant Nos. 12373033, 12090040/4, 12373033, 12373036, 12222305, 12427804, the National

Key R&D Program of China 2024YFA1611903, the Scientific Instrument Developing Project of the Chinese Academy of Sciences, Grant No. ZDKYYQ20220009, the Key Project of Zhejiang Provincial Natural Science Foundation (No. ZCLZ25A0301), and the International Partnership Program of the Chinese Academy of Sciences, Grant No. 178GJHZ2022047GC.

## REFERENCES

- Balachandran, S. 1995, *ApJ*, 446, 203, doi: [10.1086/175779](https://doi.org/10.1086/175779)
- Bodenheimer, P. 1965, *ApJ*, 142, 451, doi: [10.1086/148310](https://doi.org/10.1086/148310)
- Boesgaard, A. M., Lum, M. G., & Deliyannis, C. P. 2020, *Astronomical Journal*, 160, 28, doi: [10.3847/1538-3881/ab8d31](https://doi.org/10.3847/1538-3881/ab8d31)
- Boesgaard, A. M., Stephens, A., & Deliyannis, C. P. 2005, *Astrophysical Journal*, 621, 991, doi: [10.1086/427398](https://doi.org/10.1086/427398)
- Boesgaard, A. M., & Tripicco, M. J. 1986, *ApJL*, 302, L49, doi: [10.1086/184635](https://doi.org/10.1086/184635)
- Buder, S., Sharma, S., Kos, J., et al. 2021, *MNRAS*, 506, 150, doi: [10.1093/mnras/stab1242](https://doi.org/10.1093/mnras/stab1242)
- Buder, S., Sharma, S., Kos, J., et al. 2021, *Monthly Notices of the Royal Astronomical Society*, 506, 150, doi: [10.1093/mnras/stab1242](https://doi.org/10.1093/mnras/stab1242)
- Buder, S., Kos, J., Wang, E. X., et al. 2024, *Publications of the Astronomical Society of Australia*, 42, e045. <https://arxiv.org/abs/2409.19858>
- . 2025, *The GALAH Survey: Data Release 4*. <https://arxiv.org/abs/2409.19858>
- Burbidge, E. M., Burbidge, G. R., Fowler, W. A., & Hoyle, F. 1957, *Rev. Mod. Phys.*, 29, 547, doi: [10.1103/RevModPhys.29.547](https://doi.org/10.1103/RevModPhys.29.547)
- Cummings, J. D., Deliyannis, C. P., Maderak, R. M., & Steinhauer, A. 2017, *AJ*, 153, 128, doi: [10.3847/1538-3881/aa5b86](https://doi.org/10.3847/1538-3881/aa5b86)
- Deliyannis, C. P., Boesgaard, A. M., & King, J. R. 1998, *Astrophysical Journal Letters*, 498, L147, doi: [10.1086/311318](https://doi.org/10.1086/311318)
- Deliyannis, C. P., Demarque, P., & Kawaler, S. D. 1990, *ApJS*, 73, 21, doi: [10.1086/191439](https://doi.org/10.1086/191439)
- Deliyannis, C. P., King, J. R., Boesgaard, A. M., & Ryan, S. G. 1994, *ApJL*, 434, L71, doi: [10.1086/187577](https://doi.org/10.1086/187577)
- El-Badry, K., & Rix, H.-W. 2018, *MNRAS*, 480, 4884, doi: [10.1093/mnras/sty2186](https://doi.org/10.1093/mnras/sty2186)
- El-Badry, K., Rix, H.-W., & Heintz, T. M. 2021, *MNRAS*, 506, 2269, doi: [10.1093/mnras/stab323](https://doi.org/10.1093/mnras/stab323)
- Gaia Collaboration, Brown, A. G. A., Vallenari, A., et al. 2021, *A&A*, 650, C3, doi: [10.1051/0004-6361/202039657e](https://doi.org/10.1051/0004-6361/202039657e)
- Garcia Lopez, R. J., & Spruit, H. C. 1991, *ApJ*, 377, 268, doi: [10.1086/170356](https://doi.org/10.1086/170356)
- Gustafsson, B., Edvardsson, B., Eriksson, K., et al. 2008, *A&A*, 486, 951, doi: [10.1051/0004-6361:200809724](https://doi.org/10.1051/0004-6361:200809724)
- Hawkins, K., Lucey, M., Ting, Y.-S., et al. 2020, *MNRAS*, 492, 1164, doi: [10.1093/mnras/stz3132](https://doi.org/10.1093/mnras/stz3132)
- Kane, S. G., Kaczmarek, Z., Garner, A., et al. 2025, arXiv:2512.02125 [astro-ph.GA]. <https://doi.org/10.5281/zenodo.17737173>
- Li, L., Shao, Z., Li, Z.-Z., et al. 2020, *ApJ*, 901, 49, doi: [10.3847/1538-4357/abaef3](https://doi.org/10.3847/1538-4357/abaef3)
- Li, X.-F., Shi, J.-R., Li, Y., et al. 2025, *ApJ*, 990, 224, doi: [10.3847/1538-4357/adf6b3](https://doi.org/10.3847/1538-4357/adf6b3)
- Mashonkina, L., Gehren, T., Shi, J.-R., Korn, A. J., & Grupp, F. 2011, *A&A*, 528, A87, doi: [10.1051/0004-6361/201015336](https://doi.org/10.1051/0004-6361/201015336)
- Nagar, T., Spina, L., & Karakas, A. I. 2019, *The Astrophysical Journal Letters*, 888, L9, doi: [10.3847/2041-8213/ab5dc6](https://doi.org/10.3847/2041-8213/ab5dc6)
- Pinsonneault, M. 1997, *ARA&A*, 35, 557, doi: [10.1146/annurev.astro.35.1.557](https://doi.org/10.1146/annurev.astro.35.1.557)
- Pinsonneault, M. H., Kawaler, S. D., Sofia, S., & Demarque, P. 1989, *ApJ*, 338, 424, doi: [10.1086/167210](https://doi.org/10.1086/167210)
- Piskunov, N., & Valenti, J. A. 2017, *Astronomy & Astrophysics*, 597, A16, doi: [10.1051/0004-6361/201629124](https://doi.org/10.1051/0004-6361/201629124)
- Reetz, J. K. 1999, PhD thesis, Ludwig-Maximilians University of Munich, Germany
- Richer, M. G. 1993, *ApJ*, 415, 240, doi: [10.1086/173159](https://doi.org/10.1086/173159)
- Ryan, S. G. 2000, *The Newsletter of the Isaac Newton Group of Telescopes*, 3, 14
- Ryan, S. G., & Deliyannis, C. P. 1995, *ApJ*, 453, 819, doi: [10.1086/176444](https://doi.org/10.1086/176444)
- Rybicki, G. B., & Hummer, D. G. 1991, *A&A*, 245, 171
- . 1992, *A&A*, 262, 209
- Sevilla, J., Behmard, A., & Fuller, J. 2022, *MNRAS*, 516, 3354, doi: [10.1093/mnras/stac2436](https://doi.org/10.1093/mnras/stac2436)

- Shi, J. R., Gehren, T., Zhang, H. W., Zeng, J. L., & Zhao, G. 2007, *A&A*, 465, 587,  
doi: [10.1051/0004-6361:20066709](https://doi.org/10.1051/0004-6361:20066709)
- Soderblom, D. R., Jones, B. F., Balachandran, S., et al. 1993, *AJ*, 106, 1059, doi: [10.1086/116704](https://doi.org/10.1086/116704)
- Steinhauer, A., & Deliyannis, C. P. 2025, *Astrophysical Journal Letters*, 995, L21,  
doi: [10.3847/2041-8213/adxxxx](https://doi.org/10.3847/2041-8213/adxxxx)
- Sun, Q., Deliyannis, C. P., Steinhauer, A., Anthony-Twarog, B. J., & Twarog, B. A. 2023, *ApJ*, 952, 71, doi: [10.3847/1538-4357/acc5e3](https://doi.org/10.3847/1538-4357/acc5e3)
- Sun, Q., Ting, Y.-S., Anthony-Twarog, B. J., et al. 2025a, *ApJ*, 991, 185, doi: [10.3847/1538-4357/adfccd](https://doi.org/10.3847/1538-4357/adfccd)
- Sun, Q., Ting, Y.-S., Liu, F., et al. 2025b, *ApJ*, 978, 107, doi: [10.3847/1538-4357/ad8dc3](https://doi.org/10.3847/1538-4357/ad8dc3)
- Théado, S., & Vauclair, S. 2003, *ApJ*, 587, 795, doi: [10.1086/368261](https://doi.org/10.1086/368261)
- Tian, H.-J., El-Badry, K., Rix, H.-W., & Gould, A. 2020, *ApJS*, 246, 4, doi: [10.3847/1538-4365/ab54c4](https://doi.org/10.3847/1538-4365/ab54c4)

## APPENDIX

Table [A1](#) lists the stellar parameters of the binaries used in this study, including the coordinates, astrometry, atmospheric parameters and Li abundances. The complete version of this table is available in the online Journal in the machine-readable table format.

Table A1. The Coordinates, Astrometry, Atmospheric Parameters and Li Abundances of the Binaries

Name	GALAH ID	RA (deg)	DEC (deg)	$\mu_{\alpha^*}$ (mas/yr)	$\mu_{\delta}$ (mas)	$\pi$ (mas)	$M_G$	$G_{BP-RP}$ (mag)	$T_{\text{eff}}$ (K)	$\log g$	[Fe/H] (dex)	$\xi_t$	$R_V$ (km s $^{-1}$ )	$v \sin i$	A(Li) (dex)
WB01a	161212001601321	74.01	-62.05	-3.78±0.01	-6.88±0.02	1.17±0.01	2.89	0.60	6431±82	4.0±0.2	-0.20±0.08	1.5	4.0±0.5	13.0±2.3	2.84
WB01b	171104002301321	74.01	-62.05	-3.92±0.02	-6.89±0.02	1.19±0.01	3.33	0.59	6438±84	4.1±0.2	-0.20±0.09	1.5	5.1±0.6	16.0±2.3	1.50
WB02a	161217002601243	65.66	-60.09	2.41±0.01	-6.73±0.01	2.06±0.01	2.55	0.66	6188±74	3.9±0.2	-0.21±0.05	1.4	23.7±0.4	10.0±2.1	1.49
WB02b	161217002601252	65.71	-60.10	2.41±0.01	-6.72±0.01	2.06±0.01	4.15	0.70	6107±96	4.3±0.2	-0.17±0.10	1.3	23.9±0.6	6.9±2.4	2.46
WB03a	150411006101052	249.46	-19.92	-6.21±0.02	-9.54±0.02	1.80±0.02	3.74	1.35	6017±84	3.7±0.2	-0.01±0.07	1.3	-22.5±0.4	7.7±2.2	1.03
WB03b	150411006101048	249.48	-19.90	-6.29±0.06	-9.61±0.04	1.87±0.05	4.39	1.47	6180±90	3.9±0.2	-0.10±0.09	1.4	-22.1±0.5	9.0±2.3	2.47
WB04a	181226002601276	69.92	3.99	-2.01±0.02	-4.33±0.01	1.24±0.02	3.25	0.97	6094±79	3.9±0.2	0.11±0.06	1.3	16.4±0.4	10.3±2.2	1.44
WB04b	181226002601213	69.91	3.98	-2.07±0.02	-4.38±0.01	1.26±0.02	3.91	0.94	6178±84	4.2±0.2	0.11±0.07	1.4	16.3±0.5	12.3±2.2	1.98
WB05a	151111001601396	339.76	-5.26	35.22±0.02	-50.42±0.02	4.52±0.02	3.80	0.83	5892±72	4.2±0.2	0.30±0.05	1.2	-30.9±0.3	6.3±2.1	2.89
WB05b	151111001601399	339.73	-5.25	35.31±0.03	-50.40±0.02	4.53±0.02	4.62	0.86	5746±78	4.4±0.2	0.23±0.05	1.1	-31.1±0.4	6.8±2.1	1.38
WB06a	160112001601101	124.17	16.31	28.72±0.03	-17.40±0.02	2.89±0.03	2.62	0.81	5743±70	3.7±0.2	-0.03±0.04	1.1	25.3±0.3	7.2±2.1	1.69
WB06b	160108003101098	124.19	16.31	28.82±0.02	-17.25±0.02	2.86±0.03	6.38	1.23	4705±121	4.6±0.2	0.03±0.11	1	26.1±0.6	6.2±2.5	0.77
WB07a	151008004001147	65.42	18.01	7.88±0.02	-16.25±0.02	3.00±0.01	5.30	1.23	5679±98	4.3±0.2	-0.05±0.08	1.1	47.8±0.5	4.5±2.4	1.75
WB07b	151008004001149	65.41	18.01	7.89±0.02	-16.34±0.01	3.00±0.01	5.30	1.21	5698±98	4.3±0.2	0.04±0.09	1.1	47.7±0.5	6.6±2.4	2.01
WB08a	160112001601232	123.38	17.26	-30.24±0.02	-22.43±0.01	7.27±0.02	5.42	0.92	5419±76	4.5±0.2	-0.08±0.05	1.1	5.0±0.3	5.4±2.1	0.97
WB08b	160112001601228	123.37	17.25	-29.79±0.02	-22.21±0.01	7.26±0.02	5.84	1.02	5192±83	4.6±0.2	-0.02±0.06	1.1	5.0±0.4	5.7±2.2	0.97
WB09a	160106002601024	59.41	18.52	9.11±0.03	-5.01±0.02	1.85±0.03	3.71	0.91	6561±95	4.1±0.2	-0.24±0.16	1.7	-4.5±1.9	36.2±3.6	2.65
WB09b	160113001601020	59.42	18.53	9.32±0.03	-4.78±0.02	1.75±0.03	5.68	1.21	5444±158	4.4±0.2	-0.14±0.15	1.1	-2.5±0.8	6.0±2.9	1.69
WB10a	170417004001108	176.36	-39.77	-2.03±0.02	-10.02±0.01	1.11±0.01	3.57	0.93	5943±90	4.0±0.2	-0.07±0.08	1.2	20.7±0.5	6.9±2.3	1.76
WB10b	170417004001099	176.38	-39.76	-2.03±0.02	-10.02±0.01	1.12±0.02	3.93	0.86	6004±97	4.2±0.2	-0.14±0.10	1.3	21.1±0.6	9.2±2.4	2.33
WB11a	180628004301140	328.20	-4.76	-16.91±0.02	-23.99±0.02	3.29±0.02	4.72	0.83	5718±78	4.4±0.2	0.13±0.05	1.1	21.8±0.4	5.1±2.2	1.66
WB11b	180628004301138	328.26	-4.72	-16.96±0.09	-23.81±0.07	3.08±0.08	5.37	1.18	4949±90	4.5±0.2	0.16±0.07	1	20.1±0.4	7.1±2.2	0.79
WB12a	161117003001291	17.16	-62.09	-20.23±0.02	-5.44±0.01	2.90±0.01	5.08	0.90	5609±92	4.4±0.2	-0.17±0.08	1.1	2.3±0.5	7.5±2.3	1.55
WB12b	161117003001295	17.19	-62.12	-20.31±0.02	-5.47±0.02	2.87±0.01	5.26	0.88	5505±94	4.5±0.2	-0.24±0.08	1.1	2.0±0.5	6.1±2.3	0.85
WB13a	170906003602008	324.43	-54.24	16.62±0.01	0.09±0.01	3.23±0.01	4.73	0.86	5596±74	4.4±0.2	0.03±0.05	1.1	-4.2±0.3	4.5±2.1	0.83
WB13b	170906003602009	324.43	-54.25	16.78±0.01	0.15±0.01	3.23±0.01	5.85	1.09	5037±82	4.5±0.2	0.05±0.06	1	-4.4±0.4	5.5±2.2	0.73
WB14a	140609004901238	325.21	-57.71	36.01±0.01	-51.78±0.01	5.06±0.01	5.59	0.99	5227±87	4.5±0.2	0.05±0.06	1.1	2.3±0.4	4.4±2.2	1.09
WB14b	140609004901226	325.20	-57.71	36.03±0.01	-51.99±0.01	5.02±0.01	7.04	1.48	4531±115	4.6±0.2	-0.12±0.12	0.9	1.8±0.6	7.1±2.5	0.55

NOTE—The GALAH DR3 identifiers of each star are given in column 2. The coordinates are given in the column 3 and 4. The column 5 to 6 represent the proper motion at RA and DEC. The effective temperatures ( $T_{\text{eff}}$ ), the logarithmic of the surface gravity ( $\log g$ ) and the metallicity ([Fe/H]) with their errors in column 10, 11 and 12, respectively. The Microturbulence, the radial velocity, and the project rotational velocity are in the column 13 to 15. The A(Li) we measured are in the last column in this table.

**Table A1.** The Coordinates, Astrometry, Atmospheric Parameters and Li Abundances of the Binaries

Name	GALAH ID	RA (deg)	DEC (deg)	$\mu_{\alpha^*}$ (mas/yr)	$\mu_{\delta}$ (mas/yr)	$\pi$ (mas)	$M_G$	$G_{BP-RP}$ (mag)	$T_{\text{eff}}$ (K)	$\log g$	[Fe/H] (dex)	$\xi_t$	$R_V$ (km s $^{-1}$ )	$v \sin i$	A(Li) (dex)
WB15a	161228002501291	127.04	17.76	-4.57±0.02	-6.20±0.01	2.53±0.01	4.56	0.85	5741±109	4.4±0.2	0.17±0.11	1.1	45.7±0.6	7.7±2.5	1.68
WB15b	160110002601291	127.04	17.77	-4.50±0.02	-6.34±0.01	2.48±0.02	4.96	0.91	5468±118	4.4±0.2	0.18±0.12	1.1	45.4±0.6	7.8±2.5	1.65
WB16a	161006004901134	16.93	-1.73	-4.92±0.02	-18.02±0.02	1.39±0.02	4.52	0.83	5796±97	4.3±0.2	-0.41±0.09	1.2	-20.3±0.6	6.6±2.5	2.00
WB16b	161006004901129	16.94	-1.73	-5.03±0.03	-17.95±0.02	1.28±0.03	5.33	0.99	5356±124	4.3±0.2	-0.39±0.11	1.1	-19.9±0.6	4.7±2.7	1.40
WB17a	150827002901326	284.14	-53.67	1.69±0.01	-13.07±0.01	2.27±0.01	3.91	0.71	6263±111	4.3±0.2	-0.09±0.13	1.4	-14.9±0.8	10.8±2.6	2.83
WB17b	160812003101336	284.13	-53.67	2.13±0.01	-12.92±0.01	2.29±0.02	5.68	1.02	5298±104	4.5±0.2	-0.02±0.08	1.1	-15.2±0.5	5.8±2.3	1.21
WB18a	140314002601294	109.60	-64.69	-13.18±0.01	33.05±0.01	4.23±0.01	5.33	0.96	5433±74	4.5±0.2	0.20±0.05	1.1	9.5±0.3	6.0±2.1	0.95
WB18b	140314002601297	109.66	-64.70	-13.14±0.01	33.03±0.01	4.22±0.01	5.44	0.98	5319±75	4.5±0.2	0.13±0.05	1.1	9.5±0.3	5.7±2.1	1.18
WB19a	171102004501355	71.21	6.11	-1.94±0.02	-3.52±0.01	2.22±0.01	3.83	0.78	6279±78	4.2±0.2	-0.17±0.06	1.4	14.8±0.4	9.2±2.2	2.27
WB19b	171102004501353	71.18	6.10	-1.86±0.02	-3.42±0.01	2.17±0.01	4.91	0.95	5931±116	4.5±0.2	-0.02±0.11	1.2	14.3±0.7	7.2±2.6	2.22
WB20a	151008004001147	65.42	18.01	7.88±0.02	-16.25±0.02	3.00±0.01	5.30	1.23	5679±98	4.3±0.2	-0.05±0.08	1.1	47.8±0.5	4.5±2.4	1.75
WB20b	151008004001149	65.41	18.01	7.89±0.02	-16.34±0.01	3.00±0.01	5.30	1.21	5698±98	4.3±0.2	0.04±0.09	1.1	47.7±0.5	6.6±2.4	2.01
WB21a	160112001601232	123.38	17.26	-30.24±0.02	-22.43±0.01	7.27±0.02	5.42	0.92	5419±76	4.5±0.2	-0.08±0.05	1.1	5.0±0.3	5.4±2.1	0.97
WB21b	160112001601228	123.37	17.25	-29.79±0.02	-22.21±0.01	7.26±0.02	5.84	1.02	5192±83	4.6±0.2	-0.02±0.06	1.1	5.0±0.4	5.7±2.2	0.97
WB22a	160106002601024	59.41	18.52	9.11±0.03	-5.01±0.02	1.85±0.03	3.71	0.91	6561±95	4.1±0.2	-0.24±0.16	1.7	-4.5±1.9	36.2±3.6	2.65
WB22b	160113001601020	59.42	18.53	9.32±0.03	-4.78±0.02	1.75±0.03	5.68	1.21	5444±158	4.4±0.2	-0.14±0.15	1.1	-2.5±0.8	6.0±2.9	1.69
WB23a	170417004001108	176.36	-39.77	-2.03±0.02	-10.02±0.01	1.11±0.01	3.57	0.93	5943±90	4.0±0.2	-0.07±0.08	1.2	20.7±0.5	6.9±2.3	1.76
WB23b	170417004001099	176.38	-39.76	-2.03±0.02	-10.02±0.01	1.12±0.02	3.93	0.86	6004±97	4.2±0.2	-0.14±0.10	1.3	21.1±0.6	9.2±2.4	2.33
WB24a	180628004301140	328.20	-4.76	-16.91±0.02	-23.99±0.02	3.29±0.02	4.72	0.83	5718±78	4.4±0.2	0.13±0.05	1.1	21.8±0.4	5.1±2.2	1.66
WB24b	180628004301138	328.26	-4.72	-16.96±0.09	-23.81±0.07	3.08±0.08	5.37	1.18	4949±90	4.5±0.2	0.16±0.07	1	20.1±0.4	7.1±2.2	0.79
WB25a	161117003001291	17.16	-62.09	-20.23±0.02	-5.44±0.01	2.90±0.01	5.08	0.90	5609±92	4.4±0.2	-0.17±0.08	1.1	2.3±0.5	7.5±2.3	1.55
WB25b	161117003001295	17.19	-62.12	-20.31±0.02	-5.47±0.02	2.87±0.01	5.26	0.88	5505±94	4.5±0.2	-0.24±0.08	1.1	2.0±0.5	6.1±2.3	0.85
WB26a	170906003602008	324.43	-54.24	16.62±0.01	0.09±0.01	3.23±0.01	4.73	0.86	5596±74	4.4±0.2	0.03±0.05	1.1	-4.2±0.3	4.5±2.1	0.83
WB26b	170906003602009	324.43	-54.25	16.78±0.01	0.15±0.01	3.23±0.01	5.85	1.09	5037±82	4.5±0.2	0.05±0.06	1	-4.4±0.4	5.5±2.2	0.73
WB27a	140609004901238	325.21	-57.71	36.01±0.01	-51.78±0.01	5.06±0.01	5.59	0.99	5227±87	4.5±0.2	0.05±0.06	1.1	2.3±0.4	4.4±2.2	1.09
WB27b	140609004901226	325.20	-57.71	36.03±0.01	-51.99±0.01	5.02±0.01	7.04	1.48	4531±115	4.6±0.2	-0.12±0.12	0.9	1.8±0.6	7.1±2.5	0.55
WB28a	161228002501291	127.04	17.76	-4.57±0.02	-6.20±0.01	2.53±0.01	4.56	0.85	5741±109	4.4±0.2	0.17±0.11	1.1	45.7±0.6	7.7±2.5	1.68
WB28b	160110002601291	127.04	17.77	-4.50±0.02	-6.34±0.01	2.48±0.02	4.96	0.91	5468±118	4.4±0.2	0.18±0.12	1.1	45.4±0.6	7.8±2.5	1.65
WB29a	161006004901134	16.93	-1.73	-4.92±0.02	-18.02±0.02	1.39±0.02	4.52	0.83	5796±97	4.3±0.2	-0.41±0.09	1.2	-20.3±0.6	6.6±2.5	2.00
WB29b	161006004901129	16.94	-1.73	-5.03±0.03	-17.95±0.02	1.28±0.03	5.33	0.99	5356±124	4.3±0.2	-0.39±0.11	1.1	-19.9±0.6	4.7±2.7	1.40

Table A1. The Coordinates, Astrometry, Atmospheric Parameters and Li Abundances of the Binaries

Name	GALAH ID	RA (deg)	DEC (deg)	$\mu_{\alpha^*}$ (mas/yr)	$\mu_{\delta}$ (mas/yr)	$\pi$ (mas)	$M_G$	$G_{BP-RP}$ (mag)	$T_{\text{eff}}$ (K)	$\log g$	[Fe/H] (dex)	$\xi_t$	$R_V$ (km s $^{-1}$ )	$v \sin i$	A(Li) (dex)
WB30a	150827002901326	284.14	-53.67	1.69±0.01	-13.07±0.01	2.27±0.01	3.91	0.71	6263±111	4.3±0.2	-0.09±0.13	1.4	-14.9±0.8	10.8±2.6	2.83
WB30b	160812003101336	284.13	-53.67	2.13±0.01	-12.92±0.01	2.29±0.02	5.68	1.02	5298±104	4.5±0.2	-0.02±0.08	1.1	-15.2±0.5	5.8±2.3	1.21
WB31a	140314002601294	109.60	-64.69	-13.18±0.01	33.05±0.01	4.23±0.01	5.33	0.96	5433±74	4.5±0.2	0.20±0.05	1.1	9.5±0.3	6.0±2.1	0.95
WB31b	140314002601297	109.66	-64.70	-13.14±0.01	33.03±0.01	4.22±0.01	5.44	0.98	5319±75	4.5±0.2	0.13±0.05	1.1	9.5±0.3	5.7±2.1	1.18
WB32a	171102004501355	71.21	6.11	-1.94±0.02	-3.52±0.01	2.22±0.01	3.83	0.78	6279±78	4.2±0.2	-0.17±0.06	1.4	14.8±0.4	9.2±2.2	2.27
WB32b	171102004501353	71.18	6.10	-1.86±0.02	-3.42±0.01	2.17±0.01	4.91	0.95	5931±116	4.5±0.2	-0.02±0.11	1.2	14.3±0.7	7.2±2.6	2.22
WB33a	151008004001147	65.42	18.01	7.88±0.02	-16.25±0.02	3.00±0.01	5.30	1.23	5679±98	4.3±0.2	-0.05±0.08	1.1	47.8±0.5	4.5±2.4	1.75
WB33b	151008004001149	65.41	18.01	7.89±0.02	-16.34±0.01	3.00±0.01	5.30	1.21	5698±98	4.3±0.2	0.04±0.09	1.1	47.7±0.5	6.6±2.4	2.01
WB34a	160112001601232	123.38	17.26	-30.24±0.02	-22.43±0.01	7.27±0.02	5.42	0.92	5419±76	4.5±0.2	-0.08±0.05	1.1	5.0±0.3	5.4±2.1	0.97
WB34b	160112001601228	123.37	17.25	-29.79±0.02	-22.21±0.01	7.26±0.02	5.84	1.02	5192±83	4.6±0.2	-0.02±0.06	1.1	5.0±0.4	5.7±2.2	0.97
WB35a	160106002601024	59.41	18.52	9.11±0.03	-5.01±0.02	1.85±0.03	3.71	0.91	6561±95	4.1±0.2	-0.24±0.16	1.7	-4.5±1.9	36.2±3.6	2.65
WB35b	160113001601020	59.42	18.53	9.32±0.03	-4.78±0.02	1.75±0.03	5.68	1.21	5444±158	4.4±0.2	-0.14±0.15	1.1	-2.5±0.8	6.0±2.9	1.69
WB36a	170417004001108	176.36	-39.77	-2.03±0.02	-10.02±0.01	1.11±0.01	3.57	0.93	5943±90	4.0±0.2	-0.07±0.08	1.2	20.7±0.5	6.9±2.3	1.76
WB36b	170417004001099	176.38	-39.76	-2.03±0.02	-10.02±0.01	1.12±0.02	3.93	0.86	6004±97	4.2±0.2	-0.14±0.10	1.3	21.1±0.6	9.2±2.4	2.33
WB37a	180628004301140	328.20	-4.76	-16.91±0.02	-23.99±0.02	3.29±0.02	4.72	0.83	5718±78	4.4±0.2	0.13±0.05	1.1	21.8±0.4	5.1±2.2	1.66
WB37b	180628004301138	328.26	-4.72	-16.96±0.09	-23.81±0.07	3.08±0.08	5.37	1.18	4949±90	4.5±0.2	0.16±0.07	1	20.1±0.4	7.1±2.2	0.79
WB38a	161117003001291	17.16	-62.09	-20.23±0.02	-5.44±0.01	2.90±0.01	5.08	0.90	5609±92	4.4±0.2	-0.17±0.08	1.1	2.3±0.5	7.5±2.3	1.55
WB38b	161117003001295	17.19	-62.12	-20.31±0.02	-5.47±0.02	2.87±0.01	5.26	0.88	5505±94	4.5±0.2	-0.24±0.08	1.1	2.0±0.5	6.1±2.3	0.85
WB39a	170906003602008	324.43	-54.24	16.62±0.01	0.09±0.01	3.23±0.01	4.73	0.86	5596±74	4.4±0.2	0.03±0.05	1.1	-4.2±0.3	4.5±2.1	0.83
WB39b	170906003602009	324.43	-54.25	16.78±0.01	0.15±0.01	3.23±0.01	5.85	1.09	5037±82	4.5±0.2	0.05±0.06	1	-4.4±0.4	5.5±2.2	0.73
WB40a	140609004901238	325.21	-57.71	36.01±0.01	-51.78±0.01	5.06±0.01	5.59	0.99	5227±87	4.5±0.2	0.05±0.06	1.1	2.3±0.4	4.4±2.2	1.09
WB40b	140609004901226	325.20	-57.71	36.03±0.01	-51.99±0.01	5.02±0.01	7.04	1.48	4531±115	4.6±0.2	-0.12±0.12	0.9	1.8±0.6	7.1±2.5	0.55
WB41a	161228002501291	127.04	17.76	-4.57±0.02	-6.20±0.01	2.53±0.01	4.56	0.85	5741±109	4.4±0.2	0.17±0.11	1.1	45.7±0.6	7.7±2.5	1.68
WB41b	160110002601291	127.04	17.77	-4.50±0.02	-6.34±0.01	2.48±0.02	4.96	0.91	5468±118	4.4±0.2	0.18±0.12	1.1	45.4±0.6	7.8±2.5	1.65
WB42a	161006004901134	16.93	-1.73	-4.92±0.02	-18.02±0.02	1.39±0.02	4.52	0.83	5796±97	4.3±0.2	-0.41±0.09	1.2	-20.3±0.6	6.6±2.5	2.00
WB42b	161006004901129	16.94	-1.73	-5.03±0.03	-17.95±0.02	1.28±0.03	5.33	0.99	5356±124	4.3±0.2	-0.39±0.11	1.1	-19.9±0.6	4.7±2.7	1.40
WB43a	151110001601020	343.01	-13.75	-9.74±0.03	-11.02±0.02	2.04±0.02	1.55	0.64	6312±70	3.6±0.2	-0.23±0.05	1.4	1.2±0.5	37.2±2.1	2.63
WB43b	151110001601394	342.99	-13.75	-9.64±0.03	-10.96±0.02	1.96±0.02	2.91	0.57	6567±76	4.1±0.2	-0.26±0.08	1.7	2.9±0.8	31.5±2.3	2.28
WB44a	151110001601243	342.43	-13.43	43.60±0.02	-49.37±0.01	4.35±0.02	4.03	0.84	5824±75	4.2±0.2	0.32±0.05	1.2	-10.5±0.3	6.0±2.1	2.73
WB44b	151110002101228	342.41	-13.45	43.48±0.02	-49.04±0.02	4.32±0.02	7.01	1.54	4466±92	4.6±0.2	0.26±0.08	0.9	-9.8±0.4	5.5±2.3	0.12

**Table A1.** The Coordinates, Astrometry, Atmospheric Parameters and Li Abundances of the Binaries

Name	GALAH ID	RA (deg)	DEC (deg)	$\mu_{\alpha^*}$ (mas/yr)	$\mu_{\delta}$ (mas)	$\pi$ (mas)	$M_G$	$G_{BP-RP}$ (mag)	$T_{\text{eff}}$ (K)	$\log g$	[Fe/H] (dex)	$\xi_t$	$R_V$ (km s <sup>-1</sup> )	$v \sin i$	A(Li) (dex)
WB45a	141104002301335	338.53	-13.25	-7.82±0.02	-21.61±0.02	4.08±0.02	6.09	1.25	4967±88	4.6±0.2	0.41±0.07	1	-14.2±0.4	6.4±2.2	0.80
WB45b	141104002301275	338.52	-13.25	-7.79±0.02	-21.90±0.02	4.11±0.02	6.60	1.41	4717±97	4.6±0.2	0.37±0.09	1	-14.1±0.5	5.7±2.3	0.49
WB46a	141104002301070	338.95	-14.11	1.25±0.02	5.12±0.01	3.43±0.02	5.22	0.89	5496±85	4.5±0.2	-0.11±0.06	1.1	7.6±0.4	7.7±2.2	1.88
WB46b	141104002301072	338.93	-14.12	1.24±0.02	5.15±0.02	3.45±0.02	6.52	1.23	4747±107	4.6±0.2	-0.06±0.09	1	7.5±0.5	6.9±2.4	0.65
WB47a	140711003401166	330.76	-8.45	62.22±0.02	0.71±0.01	6.15±0.02	6.47	1.28	4765±77	4.6±0.2	0.19±0.05	1	-23.3±0.3	5.6±2.1	0.04
WB47b	140711003401005	330.79	-8.41	62.40±0.02	0.87±0.02	6.16±0.02	6.73	1.36	4635±81	4.6±0.2	0.14±0.06	1	-23.2±0.4	6.1±2.2	0.01
WB48a	140708005301013	333.84	-6.85	3.39±0.02	12.90±0.02	1.17±0.02	3.46	1.06	5061±182	3.7±0.2	-0.15±0.14	1.1	-42.5±0.7	7.3±2.6	1.45
WB48b	151009002601014	333.84	-6.86	3.37±0.02	13.03±0.02	1.19±0.02	3.72	0.80	5845±105	4.0±0.2	-0.14±0.10	1.2	-43.0±0.6	6.0±2.5	2.25
WB49a	140708005301144	332.82	-6.90	31.97±0.02	-9.10±0.02	2.91±0.02	6.21	1.23	4873±118	4.5±0.2	0.02±0.10	1	6.8±0.5	6.3±2.4	1.03
WB49b	151009002601139	332.82	-6.91	31.90±0.02	-9.30±0.02	2.95±0.02	6.28	1.25	4833±103	4.6±0.2	0.16±0.09	1	6.6±0.5	6.1±2.4	0.83
WB50a	170603005601010	257.79	-21.75	3.82±0.02	0.29±0.01	1.95±0.02	1.60	1.52	4838±77	2.5±0.2	-0.02±0.05	1.2	8.7±0.3	6.9±2.1	0.65
WB50b	170603005601008	257.80	-21.74	3.73±0.02	0.24±0.01	1.92±0.02	1.69	1.51	4857±79	2.5±0.2	-0.03±0.05	1.2	8.0±0.3	6.4±2.1	0.60
WB51a	170506002401206	142.31	-70.41	-3.34±0.01	5.36±0.01	2.72±0.01	3.79	0.75	6381±88	4.3±0.2	0.08±0.09	1.5	-7.3±0.6	14.8±2.3	2.60
WB51b	170506002401222	142.33	-70.40	-3.35±0.01	5.36±0.01	2.69±0.01	3.84	0.74	6320±101	4.3±0.2	0.04±0.11	1.5	-7.8±0.8	14.5±2.5	2.99
WB52a	151109002101145	22.28	5.80	-8.57±0.02	-9.81±0.01	1.77±0.02	3.58	0.67	6234±83	4.2±0.2	-0.25±0.08	1.4	-4.6±0.5	7.9±2.3	2.08
WB52b	170724005101147	22.28	5.81	-8.76±0.03	-9.75±0.02	1.70±0.03	5.59	0.99	5242±136	4.5±0.2	-0.10±0.12	1.1	-4.8±0.6	5.6±2.6	1.39
WB53a	151109002101230	22.02	6.58	-15.49±0.02	-14.84±0.01	3.95±0.02	5.12	0.95	5472±79	4.5±0.2	0.30±0.05	1.1	-13.1±0.4	5.6±2.2	1.20
WB53b	170723005101228	22.02	6.57	-15.44±0.02	-14.69±0.01	3.92±0.02	6.47	1.33	4712±104	4.6±0.2	0.23±0.10	1	-13.1±0.5	4.9±2.4	0.61
WB54a	161009004301039	13.48	9.51	-3.55±0.02	-30.87±0.02	4.12±0.02	3.80	0.81	5882±75	4.1±0.2	0.19±0.05	1.2	-13.8±0.3	6.1±2.1	2.50
WB54b	161107002101042	13.47	9.50	-3.24±0.02	-30.89±0.02	4.07±0.02	6.94	1.50	4560±82	4.6±0.2	0.18±0.06	0.9	-13.5±0.4	5.2±2.2	0.23
WB55a	181224002601104	65.90	-76.72	35.14±0.01	-41.31±0.01	5.83±0.01	4.92	0.82	5540±123	4.4±0.2	-0.42±0.13	1.1	58.5±0.7	4.9±2.8	1.51
WB55b	181224002601103	65.95	-76.72	35.11±0.02	-41.20±0.02	5.79±0.02	5.00	0.83	5509±122	4.4±0.2	-0.40±0.12	1.1	58.5±0.7	4.9±2.8	1.48
WB56a	181224002601047	66.89	-76.26	-5.00±0.01	3.71±0.01	3.73±0.01	4.61	0.83	5881±80	4.4±0.2	0.05±0.06	1.2	3.3±0.4	4.9±2.2	2.36
WB56b	161011002801251	66.90	-76.26	-5.03±0.01	3.76±0.02	3.73±0.01	4.99	0.90	5715±79	4.5±0.2	0.07±0.05	1.1	3.9±0.4	6.0±2.2	1.53
WB57a	151225003801025	150.17	-33.03	32.24±0.01	-34.26±0.01	4.43±0.01	6.44	1.26	4750±97	4.6±0.2	0.15±0.08	1	13.4±0.5	5.6±2.3	0.51
WB57b	151225003801026	150.19	-33.02	32.33±0.01	-34.19±0.01	4.42±0.01	6.54	1.30	4766±95	4.6±0.2	0.08±0.08	1	13.2±0.5	6.7±2.3	-0.27
WB58a	160107002601294	26.33	-25.29	20.87±0.03	1.00±0.02	3.53±0.03	3.23	0.57	6466±74	4.1±0.2	-0.25±0.06	1.6	4.2±0.4	8.9±2.1	0.83
WB58b	160107002601291	26.31	-25.26	20.81±0.02	0.76±0.01	3.47±0.02	5.92	1.04	5161±130	4.6±0.2	-0.17±0.12	1	4.1±0.6	6.9±2.5	1.22
WB59a	160813002101209	260.08	-69.26	1.33±0.01	-7.13±0.01	1.05±0.01	3.22	0.81	5923±84	3.9±0.2	0.00±0.07	1.2	-21.7±0.4	7.2±2.2	2.31
WB59b	140710004601206	260.08	-69.26	1.29±0.01	-7.04±0.01	1.04±0.01	3.75	0.81	5979±92	4.1±0.2	0.08±0.08	1.2	-21.4±0.5	7.8±2.3	2.10

Table A1. The Coordinates, Astrometry, Atmospheric Parameters and Li Abundances of the Binaries

Name	GALAH ID	RA (deg)	DEC (deg)	$\mu_{\alpha^*}$ (mas/yr)	$\mu_{\delta}$	$\pi$ (mas)	$M_G$	$G_{BP-RP}$ (mag)	$T_{\text{eff}}$ (K)	$\log g$	[Fe/H] (dex)	$\xi_t$	$R_V$ (km s $^{-1}$ )	$v \sin i$	A(Li) (dex)
WB60a	170216003301017	190.83	-29.69	30.67±0.02	-5.65±0.01	1.80±0.02	4.87	0.90	5465±101	4.3±0.2	-0.29±0.08	1.1	0.1±0.5	4.9±2.4	1.34
WB60b	170216003301016	190.84	-29.68	30.66±0.02	-5.71±0.01	1.81±0.02	5.03	0.94	5386±104	4.4±0.2	-0.18±0.09	1.1	-0.3±0.5	4.5±2.4	1.30
WB61a	151110004201385	110.24	8.89	1.56±0.02	-4.90±0.02	1.82±0.02	2.15	0.58	6518±86	3.8±0.2	-0.10±0.10	1.6	-13.8±0.6	11.9±2.3	2.76
WB61b	151110004201386	110.23	8.87	1.60±0.02	-5.01±0.02	1.80±0.02	2.51	0.54	6630±101	4.0±0.2	-0.01±0.14	1.7	-22.6±1.3	23.1±2.8	3.03
WB62a	151110004201055	109.92	8.04	-38.11±0.02	-51.70±0.01	4.08±0.01	3.62	0.71	5991±79	4.1±0.2	-0.41±0.06	1.2	-30.2±0.4	5.1±2.2	2.38
WB62b	151110004201051	109.91	8.06	-38.22±0.02	-51.94±0.01	4.11±0.01	4.12	0.71	5980±88	4.2±0.2	-0.43±0.08	1.2	-29.4±0.5	6.3±2.3	2.15
WB63a	170506005401269	286.49	-20.23	5.57±0.02	0.88±0.02	2.23±0.02	2.83	0.72	6492±77	3.9±0.2	-0.15±0.08	1.6	-19.7±0.9	36.2±2.5	1.67
WB63b	170506005401263	286.47	-20.23	5.60±0.02	0.80±0.01	2.22±0.02	2.84	0.73	6537±77	4.0±0.2	-0.11±0.08	1.6	-20.1±0.9	35.7±2.5	2.45
WB64a	160813001601030	250.61	-67.48	-2.04±0.01	-7.88±0.01	4.59±0.02	4.29	0.72	6047±80	4.3±0.2	-0.45±0.07	1.3	18.3±0.4	6.4±2.2	2.37
WB64b	160813001601029	250.60	-67.46	-2.26±0.01	-7.67±0.02	4.57±0.02	5.16	0.85	5500±103	4.5±0.2	-0.47±0.09	1.1	18.0±0.5	4.4±2.5	1.60
WB65a	161012002601330	329.36	-69.32	5.72±0.01	0.80±0.01	3.32±0.01	5.43	0.93	5330±109	4.5±0.2	-0.23±0.10	1.1	11.0±0.5	7.5±2.4	1.17
WB65b	161012002601324	329.24	-69.32	5.83±0.02	0.84±0.02	3.36±0.02	5.56	0.96	5325±125	4.6±0.2	-0.18±0.12	1.1	15.4±0.6	6.1±2.6	1.37
WB66a	160923003701093	53.74	21.59	14.53±0.02	-3.86±0.01	2.18±0.01	3.62	0.93	6027±104	4.0±0.2	0.01±0.11	1.3	70.2±0.6	9.9±2.4	2.13
WB66b	151109002601093	53.73	21.60	14.79±0.03	-3.67±0.02	2.19±0.02	6.40	1.34	4898±134	4.5±0.2	0.01±0.12	1	69.8±0.6	4.5±2.7	0.94
WB67a	150427003302141	239.51	-20.30	18.61±0.02	-21.39±0.01	5.08±0.02	5.28	1.09	5651±73	4.4±0.2	-0.11±0.05	1.1	9.9±0.3	6.9±2.1	1.35
WB67b	150428001601143	239.49	-20.30	18.69±0.02	-21.39±0.01	5.02±0.02	6.85	1.44	4789±98	4.6±0.2	0.00±0.08	1	9.9±0.5	5.2±2.3	0.66
WB68a	170515004101280	236.52	-19.61	14.19±0.02	-3.71±0.01	1.61±0.01	2.80	1.31	4828±87	3.2±0.2	-0.01±0.06	1.2	38.4±0.4	7.0±2.2	0.92
WB68b	160518001901012	236.51	-19.62	14.21±0.02	-3.62±0.01	1.60±0.01	3.85	0.99	5679±93	4.0±0.2	0.01±0.08	1.1	38.3±0.5	6.2±2.3	2.03
WB69a	170515004101292	236.59	-19.45	-2.42±0.02	1.57±0.01	1.90±0.02	3.34	0.71	6551±81	4.1±0.2	-0.12±0.09	1.6	-29.4±0.9	29.0±2.5	1.38
WB69b	160518001901378	236.60	-19.45	-2.28±0.02	1.56±0.02	1.89±0.02	5.38	1.02	5568±143	4.5±0.2	-0.04±0.14	1.1	-29.0±0.8	8.5±2.7	1.92
WB70a	170205005901140	207.12	-47.53	-14.36±0.02	-8.51±0.02	1.98±0.02	0.89	1.15	4998±72	2.8±0.2	0.07±0.04	1.2	7.0±0.3	6.5±2.1	1.16
WB70b	160522003601131	207.22	-47.60	-14.33±0.02	-8.47±0.02	2.05±0.02	5.34	1.02	5316±111	4.4±0.2	-0.22±0.09	1.1	21.2±0.5	7.4±2.4	1.33
WB71a	150604003402184	241.82	-17.12	-1.21±0.02	-11.44±0.02	1.37±0.02	1.89	1.48	4644±74	2.6±0.2	-0.24±0.05	1.3	-60.7±0.3	6.0±2.1	0.32
WB71b	150604003401185	241.82	-17.11	-1.14±0.02	-11.44±0.02	1.33±0.02	4.03	1.07	5800±139	4.0±0.2	-0.12±0.16	1.2	-60.8±0.7	5.6±2.9	2.36
WB72a	150427004302058	242.92	-17.40	51.29±0.03	67.43±0.02	9.61±0.02	6.06	1.06	5000±74	4.6±0.2	-0.38±0.05	1	-2.3±0.3	5.2±2.1	0.27
WB72b	150604003402073	242.92	-17.38	51.60±0.03	67.38±0.02	9.65±0.02	6.27	1.13	4929±71	4.6±0.2	-0.26±0.04	1	-2.6±0.3	5.8±2.1	0.29
WB73a	170115002701376	105.21	-60.79	-6.09±0.01	9.79±0.01	1.44±0.01	2.98	0.67	6583±100	4.0±0.2	-0.50±0.26	1.7	-22.8±3.1	50.6±5.3	3.20
WB73b	170115002701375	105.16	-60.79	-6.07±0.01	9.82±0.01	1.44±0.01	3.29	0.67	6584±107	4.1±0.2	-0.37±0.18	1.7	-21.3±1.5	21.1±3.0	2.80
WB74a	170108002201232	81.49	-69.08	1.34±0.01	0.75±0.01	3.56±0.01	2.91	0.90	5671±72	3.8±0.2	0.16±0.05	1.1	24.0±0.3	5.7±2.1	1.45
WB74b	170108002201252	81.51	-69.07	1.45±0.01	0.51±0.01	3.57±0.01	3.62	0.79	6028±77	4.1±0.2	0.17±0.05	1.3	23.9±0.4	6.8±2.1	2.19

**Table A1.** The Coordinates, Astrometry, Atmospheric Parameters and Li Abundances of the Binaries

Name	GALAH ID	RA (deg)	DEC (deg)	$\mu_{\alpha^*}$ (mas/yr)	$\mu_{\delta}$ (mas/yr)	$\pi$ (mas)	$M_G$	$G_{BP-RP}$ (mag)	$T_{\text{eff}}$ (K)	$\log g$	[Fe/H] (dex)	$\xi_t$	$R_V$ (km s <sup>-1</sup> )	$v \sin i$	A(Li) (dex)
WB75a	151009004601070	61.69	13.26	11.90±0.02	-2.03±0.01	1.79±0.02	4.17	1.27	5803±112	3.8±0.2	-0.50±0.13	1.2	36.3±0.7	6.7±2.7	2.20
WB75b	160106002101085	61.69	13.26	11.97±0.03	-1.94±0.02	1.81±0.02	5.51	1.27	5735±124	4.3±0.2	-0.59±0.15	1.1	37.1±0.8	5.7±2.9	1.95
WB76a	160514003301047	228.12	-18.56	-20.97±0.02	-7.94±0.02	2.14±0.02	3.72	0.82	5916±76	4.1±0.2	-0.24±0.05	1.2	-2.0±0.4	5.9±2.2	2.32
WB76b	160514003301136	228.12	-18.54	-20.96±0.02	-7.89±0.03	2.12±0.02	4.10	0.81	5859±85	4.2±0.2	-0.37±0.07	1.2	-1.9±0.4	6.1±2.3	2.08
WB77a	190207002701019	171.83	1.65	-7.31±0.02	-16.59±0.01	2.43±0.02	4.82	0.81	5661±97	4.4±0.2	-0.25±0.08	1.1	38.6±0.5	5.7±2.4	1.78
WB77b	190207002701018	171.84	1.66	-7.22±0.02	-16.61±0.01	2.43±0.02	4.94	0.84	5544±104	4.4±0.2	-0.21±0.09	1.1	38.9±0.5	5.6±2.4	1.91
WB78a	150409005601005	174.20	1.38	4.29±0.02	3.11±0.02	1.66±0.02	3.60	0.63	6342±88	4.2±0.2	-0.23±0.09	1.5	-5.5±0.6	13.5±2.3	2.21
WB78b	150427002301018	174.20	1.38	3.99±0.02	2.96±0.02	1.63±0.02	4.12	0.71	6056±129	4.3±0.2	-0.24±0.17	1.3	-5.7±1.0	8.7±3.0	2.34
WB79a	150427001301227	167.28	-0.21	-21.48±0.02	12.45±0.02	1.64±0.02	2.74	0.76	5925±95	3.8±0.2	-0.41±0.10	1.2	10.4±0.5	6.9±2.4	1.86
WB79b	170219003101228	167.27	-0.21	-21.47±0.02	12.45±0.02	1.65±0.02	4.76	0.78	5773±103	4.4±0.2	-0.45±0.10	1.2	11.2±0.6	5.6±2.5	2.13
WB80a	171206005101090	92.41	-55.36	-5.18±0.01	11.10±0.01	3.40±0.01	5.05	0.88	5525±101	4.5±0.2	0.07±0.08	1.1	-1.0±0.5	6.1±2.3	1.56
WB80b	150207002601099	92.42	-55.36	-5.21±0.01	11.57±0.02	3.36±0.01	6.25	1.21	4877±101	4.6±0.2	0.21±0.09	1	-1.0±0.5	5.2±2.4	0.90
WB81a	150211003701379	156.73	-42.29	-45.84±0.01	21.25±0.01	4.22±0.01	5.15	0.93	5549±90	4.5±0.2	0.25±0.07	1.1	12.9±0.5	8.7±2.3	1.46
WB81b	150211003701380	156.68	-42.32	-45.86±0.01	21.40±0.01	4.24±0.01	5.49	0.99	5327±87	4.5±0.2	0.19±0.07	1.1	13.4±0.4	8.3±2.2	1.42
WB82a	140311006601008	145.27	-66.86	-27.86±0.01	15.69±0.01	1.45±0.01	4.37	0.91	6002±101	4.2±0.2	-0.56±0.12	1.3	-13.4±0.7	7.2±2.7	2.35
WB82b	160125003001387	145.30	-66.86	-27.81±0.01	15.64±0.01	1.45±0.01	4.37	0.92	5925±117	4.1±0.2	-0.36±0.14	1.2	-13.1±0.8	7.7±2.8	2.39
WB83a	150602004401252	272.08	6.80	-7.85±0.02	-6.10±0.02	1.75±0.02	4.01	1.01	6445±100	4.1±0.2	-0.02±0.11	1.6	27.6±0.6	7.9±2.5	2.37
WB83b	150601004001252	272.08	6.80	-7.65±0.02	-6.10±0.02	1.80±0.02	4.91	1.10	6097±119	4.4±0.2	-0.08±0.15	1.3	28.8±0.7	5.6±2.9	2.74
WB84a	170109003801018	111.49	-68.30	-0.81±0.02	4.73±0.01	5.94±0.01	3.96	0.67	6153±71	4.2±0.2	-0.16±0.05	1.3	30.0±0.5	37.6±2.1	2.61
WB84b	170109003801032	111.45	-68.30	-0.95±0.01	5.28±0.01	5.93±0.01	4.15	0.71	6077±72	4.4±0.2	-0.03±0.05	1.3	30.1±0.3	15.2±2.1	2.81
WB85a	150409002601096	175.82	-5.23	-7.41±0.02	2.50±0.01	2.14±0.02	3.25	0.59	6444±74	4.2±0.2	-0.08±0.06	1.6	3.9±0.6	24.6±2.2	0.94
WB85b	150409002601097	175.84	-5.22	-7.41±0.02	2.55±0.01	2.14±0.02	3.68	0.64	6286±80	4.3±0.2	-0.10±0.07	1.4	4.0±0.4	10.1±2.2	2.62
WB86a	150409002601121	175.66	-5.10	-3.36±0.02	16.51±0.01	3.92±0.02	3.68	0.68	6102±72	4.2±0.2	-0.21±0.05	1.3	9.2±0.3	7.9±2.1	2.46
WB86b	150409002601134	175.60	-5.04	-3.40±0.02	16.54±0.01	3.96±0.02	3.79	0.69	6089±72	4.2±0.2	-0.19±0.05	1.3	9.0±0.3	7.7±2.1	2.06
WB87a	150409002601340	176.18	-4.21	-19.58±0.04	17.49±0.02	1.96±0.03	3.04	0.62	6251±86	4.0±0.2	-0.34±0.09	1.4	-7.0±0.6	10.8±2.3	1.58
WB87b	150411003101336	176.18	-4.22	-19.56±0.03	17.48±0.01	1.96±0.02	4.30	0.72	5991±78	4.3±0.2	-0.21±0.06	1.2	-7.2±0.4	6.1±2.2	2.41
WB88a	160403004201140	200.53	-17.37	-7.32±0.02	-1.78±0.01	1.28±0.02	0.79	1.46	4324±72	2.2±0.2	-0.24±0.05	1.5	53.4±0.3	7.3±2.1	0.23
WB88b	170219004101139	200.54	-17.37	-7.40±0.02	-1.87±0.01	1.31±0.02	4.51	0.90	5672±143	4.3±0.2	0.17±0.16	1.1	54.1±0.8	7.4±2.8	1.94
WB89a	160423003801308	191.33	-26.02	-13.71±0.02	-61.40±0.01	2.93±0.02	4.77	0.88	5663±101	4.3±0.2	-0.40±0.09	1.1	29.1±0.6	9.4±2.4	1.63
WB89b	160423003801310	191.35	-26.02	-13.72±0.02	-61.41±0.01	2.87±0.02	5.12	0.92	5483±124	4.4±0.2	-0.49±0.12	1.1	29.3±0.8	10.5±2.6	1.65

Table A1. The Coordinates, Astrometry, Atmospheric Parameters and Li Abundances of the Binaries

Name	GALAH ID	RA (deg)	DEC (deg)	$\mu_{\alpha_*}$ (mas/yr)	$\mu_\delta$ (mas/yr)	$\pi$ (mas)	$M_G$ (mag)	$G_{BP-RP}$ (mag)	$T_{\text{eff}}$ (K)	$\log g$	[Fe/H] (dex)	$\xi_t$	$R_V$ (km s $^{-1}$ )	$v \sin i$	A(Li) (dex)
WB90a	161011003401245	65.47	-64.75	4.47±0.01	8.47±0.02	1.18±0.01	2.69	0.58	6514±76	4.0±0.2	-0.24±0.07	1.6	18.7±0.7	33.9±2.3	1.97
WB90b	161011003401246	65.40	-64.75	4.56±0.01	8.51±0.02	1.18±0.01	3.19	0.58	6543±81	4.1±0.2	-0.20±0.08	1.6	19.7±0.5	10.9±2.2	2.25
WB91a	161213003101153	65.89	-64.71	27.53±0.01	23.18±0.02	2.96±0.01	3.94	0.80	5877±76	4.2±0.2	0.20±0.05	1.2	50.1±0.3	5.8±2.1	2.05
WB91b	161011003401266	65.90	-64.71	27.42±0.01	23.05±0.02	2.98±0.01	4.40	0.85	5766±73	4.3±0.2	0.20±0.05	1.2	50.5±0.3	6.3±2.1	1.15
WB92a	181221001601191	55.96	-68.57	45.75±0.01	75.13±0.01	8.61±0.01	6.07	1.17	4944±80	4.6±0.2	0.33±0.06	1	14.5±0.4	4.4±2.2	0.68
WB92b	181221001601195	56.02	-68.51	45.86±0.01	74.93±0.01	8.64±0.01	6.83	1.44	4603±88	4.6±0.2	0.24±0.07	1	14.8±0.4	4.2±2.3	0.38
WB93a	171206001602090	62.20	-64.73	15.85±0.01	12.18±0.01	2.39±0.01	4.17	0.71	6092±70	4.3±0.2	-0.19±0.04	1.3	2.9±0.3	6.8±2.1	2.38
WB93b	171230001602367	62.19	-64.74	15.59±0.02	12.12±0.02	2.43±0.01	4.47	0.77	5982±72	4.4±0.2	-0.19±0.05	1.2	2.7±0.3	6.3±2.1	2.46
WB94a	171206002102138	63.05	-62.71	-4.67±0.01	-3.17±0.01	3.03±0.01	4.89	0.88	5618±74	4.5±0.2	0.16±0.05	1.1	33.7±0.3	6.0±2.1	1.46
WB94b	131120002501098	63.10	-62.72	-4.81±0.01	-3.18±0.01	3.03±0.01	5.83	1.10	5048±87	4.5±0.2	0.19±0.07	1	34.1±0.4	4.9±2.2	0.79
WB95a	171208001602318	64.99	-66.35	107.27±0.02	77.95±0.02	5.74±0.01	4.83	0.88	5518±70	4.4±0.2	-0.01±0.04	1.1	61.4±0.3	7.8±2.1	1.67
WB95b	160919005101273	65.00	-66.35	106.56±0.02	78.17±0.02	5.74±0.01	6.34	1.25	4656±89	4.5±0.2	0.01±0.07	1	61.4±0.4	6.4±2.2	0.43
WB96a	161213002601222	62.33	-61.77	50.00±0.01	35.60±0.01	2.92±0.01	4.57	0.85	5661±89	4.4±0.2	0.18±0.07	1.1	47.7±0.4	5.9±2.3	1.58
WB96b	171206002102222	62.33	-61.77	50.00±0.01	35.57±0.01	2.94±0.01	4.97	0.91	5540±77	4.5±0.2	0.21±0.05	1.1	47.6±0.3	5.8±2.1	1.06
WB97a	181221001601090	58.95	-69.21	20.04±0.01	26.35±0.02	3.41±0.01	3.93	0.72	6173±131	4.3±0.2	0.04±0.20	1.3	2.4±2.4	22.1±3.9	2.62
WB97b	141104003801193	58.93	-69.22	19.94±0.01	26.20±0.02	3.42±0.01	6.14	1.16	5013±132	4.6±0.2	0.01±0.12	1	2.5±0.6	6.3±2.5	1.02
WB98a	131123003001121	80.58	-62.08	9.87±0.02	47.93±0.02	4.05±0.01	6.56	1.28	4683±101	4.6±0.2	0.03±0.09	1	51.8±0.5	7.7±2.3	0.57
WB98b	131123003001162	80.55	-62.09	9.73±0.02	47.89±0.02	4.07±0.01	6.84	1.38	4464±106	4.6±0.2	-0.00±0.10	0.9	53.5±0.5	5.9±2.4	0.30
WB99a	160418002601329	140.18	-21.43	-32.13±0.01	1.72±0.01	2.42±0.01	4.00	0.79	5938±76	4.2±0.2	-0.13±0.05	1.2	19.4±0.3	6.5±2.1	2.08
WB99b	160418002601335	140.18	-21.39	-32.20±0.01	1.77±0.01	2.42±0.01	4.49	0.82	5851±81	4.3±0.2	-0.16±0.06	1.2	11.0±0.4	6.2±2.2	1.73
WB100a	140412001701261	205.11	-45.58	-8.65±0.02	-4.84±0.02	2.30±0.02	4.55	0.80	5836±87	4.3±0.2	-0.07±0.07	1.2	-17.1±0.5	8.9±2.3	2.75
WB100b	140412001701259	205.10	-45.63	-8.57±0.01	-4.77±0.01	2.34±0.02	5.28	0.92	5483±109	4.5±0.2	-0.06±0.10	1.1	-17.0±0.6	9.5±2.4	2.40
WB101a	170517002301320	205.91	-45.19	-33.74±0.02	-10.90±0.02	2.53±0.02	3.75	0.84	5919±91	4.2±0.2	0.36±0.08	1.2	-7.4±0.5	9.2±2.3	2.55
WB101b	140412001701320	205.90	-45.19	-33.59±0.01	-10.88±0.01	2.59±0.02	4.84	0.93	5579±96	4.4±0.2	0.28±0.08	1.1	-7.2±0.5	8.7±2.3	1.57
WB102a	151008002101372	293.91	-27.33	-1.47±0.02	-3.22±0.01	2.36±0.02	3.44	0.72	6476±94	4.1±0.2	-0.12±0.11	1.6	10.3±0.7	13.3±2.4	2.22
WB102b	140610005701235	293.88	-27.34	-1.63±0.02	-3.24±0.01	2.39±0.01	4.34	0.87	5925±152	4.2±0.2	-0.12±0.18	1.2	52.0±0.9	7.6±3.0	2.68
WB103a	170603006101152	281.10	-25.87	-0.10±0.02	-6.74±0.01	2.04±0.02	3.24	0.79	6867±86	4.0±0.2	0.03±0.10	2.0	-10.3±0.7	15.9±2.4	2.56
WB103b	160531004101152	281.10	-25.86	-0.15±0.02	-6.79±0.02	2.09±0.02	5.68	1.22	5490±126	4.5±0.2	0.23±0.12	1.1	-9.1±0.6	7.3±2.5	1.84
WB104a	170418001601356	147.92	-39.13	0.79±0.01	-29.48±0.01	4.07±0.01	2.58	0.72	6137±71	3.8±0.2	-0.00±0.05	1.3	-0.7±0.3	10.3±2.1	1.96
WB104b	170418001601352	147.90	-39.14	0.71±0.01	-29.55±0.02	4.05±0.02	3.90	0.72	6234±74	4.3±0.2	0.08±0.05	1.4	-0.7±0.3	7.3±2.1	2.59

**Table A1.** The Coordinates, Astrometry, Atmospheric Parameters and Li Abundances of the Binaries

Name	GALAH ID	RA (deg)	DEC (deg)	$\mu_{\alpha*}$ (mas/yr)	$\mu_{\delta}$ (mas/yr)	$\pi$ (mas)	$M_G$ (mag)	$G_{BP-RP}$ (mag)	$T_{\text{eff}}$ (K)	$\log g$	[Fe/H] (dex)	$\xi_t$	$R_V$ (km s <sup>-1</sup> )	$v \sin i$	A(Li) (dex)
WB105a	170910006101001	71.32	-65.31	-17.39±0.01	61.57±0.02	3.92±0.01	3.93	0.79	5741±75	4.1±0.2	-0.21±0.05	1.1	18.6±0.3	4.9±2.1	1.70
WB105b	161013004901159	71.31	-65.32	-17.49±0.01	61.57±0.02	3.96±0.01	6.52	1.25	4642±122	4.6±0.2	-0.18±0.12	1	19.6±0.6	6.9±2.5	0.63
WB106a	150531000901057	206.89	-78.93	-6.24±0.01	-10.12±0.01	1.85±0.01	4.42	0.85	6026±117	4.3±0.2	-0.04±0.13	1.3	-12.0±0.8	10.2±2.6	2.50
WB106b	150531000901043	206.91	-78.92	-6.29±0.01	-10.07±0.02	1.83±0.01	5.00	0.96	5732±162	4.4±0.2	-0.02±0.16	1.1	-12.1±0.9	8.7±2.9	2.10
WB107a	170109002801101	111.23	-59.66	-3.45±0.02	10.21±0.02	4.12±0.01	4.65	0.81	5834±78	4.4±0.2	0.08±0.05	1.2	26.3±0.4	6.7±2.2	2.79
WB107b	150108002201269	111.23	-59.67	-3.29±0.01	9.73±0.01	4.13±0.01	5.76	1.05	5158±108	4.6±0.2	0.08±0.08	1	26.3±0.5	7.9±2.3	1.89
WB108a	160813003101358	310.22	1.55	29.37±0.01	3.88±0.01	2.96±0.01	4.55	0.77	5929±92	4.4±0.2	-0.30±0.09	1.2	-18.1±0.5	7.6±2.3	1.96
WB108b	160813003101356	310.22	1.58	29.44±0.01	3.81±0.01	2.97±0.01	5.00	0.83	5808±107	4.5±0.2	-0.28±0.11	1.2	-17.8±0.6	6.6±2.5	1.93
WB109a	160426006701097	254.53	-76.45	1.98±0.01	3.53±0.01	3.83±0.01	5.25	0.92	5491±76	4.5±0.2	-0.05±0.05	1.1	-3.0±0.3	4.9±2.1	1.49
WB109b	160426006701102	254.49	-76.44	2.06±0.01	3.59±0.01	3.79±0.01	5.89	1.08	5002±92	4.5±0.2	-0.02±0.07	1	-2.9±0.4	4.5±2.3	1.20
WB110a	170905002601125	308.89	-47.65	7.00±0.01	-21.89±0.01	4.27±0.01	5.42	0.95	5299±81	4.5±0.2	0.07±0.05	1.1	-6.0±0.4	8.5±2.1	2.60
WB110b	170905002601123	308.90	-47.65	7.30±0.01	-21.60±0.01	4.22±0.02	6.68	1.31	4674±103	4.6±0.2	0.12±0.09	1	-5.9±0.5	4.0±2.4	1.34
WB111a	160524006101269	301.80	-44.64	-1.88±0.02	-9.09±0.01	1.52±0.02	4.47	0.77	5945±102	4.4±0.2	-0.07±0.10	1.2	-8.9±0.6	5.9±2.5	2.20
WB111b	160524006101275	301.80	-44.61	-1.85±0.02	-9.16±0.01	1.47±0.02	4.66	0.80	5869±105	4.4±0.2	-0.13±0.10	1.2	-8.7±0.6	5.9±2.5	1.94
WB112a	171228004202333	177.88	-49.35	-2.17±0.01	6.44±0.01	1.75±0.02	1.84	0.67	6288±72	3.6±0.2	-0.15±0.05	1.4	-8.6±0.3	12.4±2.1	1.87
WB112b	160524002101044	177.88	-49.34	-2.25±0.02	6.41±0.02	1.68±0.02	2.63	0.71	6072±81	3.8±0.2	-0.23±0.07	1.3	-9.2±0.5	12.5±2.2	1.94
WB113a	160130005801379	181.07	-27.69	-19.58±0.02	-2.46±0.01	1.64±0.02	4.07	0.73	6144±90	4.3±0.2	-0.11±0.08	1.3	-20.0±0.5	8.4±2.3	2.32
WB113b	160130005801392	181.07	-27.70	-19.65±0.02	-2.66±0.01	1.64±0.02	4.71	0.80	5832±106	4.4±0.2	-0.19±0.11	1.2	-20.4±0.6	5.5±2.6	2.14
WB114a	160522003101330	187.67	-35.65	-25.08±0.01	7.24±0.01	1.20±0.02	4.02	0.74	6078±98	4.2±0.2	-0.41±0.11	1.3	-56.9±0.6	8.5±2.4	2.41
WB114b	160522003101329	187.65	-35.63	-25.08±0.01	7.27±0.01	1.20±0.02	4.12	0.75	6130±115	4.3±0.2	-0.37±0.14	1.3	-56.3±0.8	6.8±2.8	2.43
WB115a	160331002701208	132.85	16.79	-6.56±0.02	-8.26±0.02	2.57±0.02	3.94	0.70	6108±77	4.3±0.2	0.01±0.06	1.3	28.7±0.4	6.3±2.2	2.56
WB115b	160112002901197	132.85	16.79	-6.71±0.02	-8.39±0.02	2.58±0.02	6.15	1.17	4895±93	4.6±0.2	0.04±0.07	1	29.0±0.4	3.9±2.3	0.76
WB116a	180622002201106	352.21	-1.68	18.46±0.03	0.36±0.02	1.65±0.02	5.36	0.97	5441±78	4.5±0.2	-0.24±0.05	1.1	1.1±0.3	4.6±2.2	1.24
WB116b	170724004601107	352.21	-1.68	18.49±0.03	0.52±0.02	1.66±0.03	5.48	0.98	5339±112	4.5±0.2	-0.21±0.10	1.1	1.0±0.5	5.1±2.5	1.40

NOTE—The GALAH DR3 identifiers of each star are given in column 2. The coordinates are given in the column 3 and 4. The column 5 to 6 represent the proper motion at RA and DEC. The effective temperatures ( $T_{\text{eff}}$ ), the logarithmic of the surface gravity ( $\log g$ ) and the metallicity ([Fe/H]) with their errors in column 10, 11 and 12, respectively. The Microturbulence, the radial velocity, and the project rotational velocity are in the column 13 to 15. The A(Li) we measured are in the last column in this table. **The complete version of this table is available in the online Journal in the machine-readable table format.**